



HAL
open science

Numerical study of non-isothermal adsorption of Naphthalene in supercritical CO₂: behavior near critical point

Manel Wannassi, Isabelle Raspo

► **To cite this version:**

Manel Wannassi, Isabelle Raspo. Numerical study of non-isothermal adsorption of Naphthalene in supercritical CO₂: behavior near critical point. *Journal of Supercritical Fluids*, 2016, 117, pp.203-218. 10.1016/j.supflu.2016.06.020 . hal-01369830

HAL Id: hal-01369830

<https://hal.science/hal-01369830>

Submitted on 6 Apr 2017

HAL is a multi-disciplinary open access archive for the deposit and dissemination of scientific research documents, whether they are published or not. The documents may come from teaching and research institutions in France or abroad, or from public or private research centers.

L'archive ouverte pluridisciplinaire **HAL**, est destinée au dépôt et à la diffusion de documents scientifiques de niveau recherche, publiés ou non, émanant des établissements d'enseignement et de recherche français ou étrangers, des laboratoires publics ou privés.

Accepted Manuscript

Title: Numerical study of non-isothermal adsorption of Naphthalene in supercritical CO₂: behavior near critical point

Author: Manel Wannassi Isabelle Raspo

PII: S0896-8446(16)30196-6
DOI: <http://dx.doi.org/doi:10.1016/j.supflu.2016.06.020>
Reference: SUPFLU 3697

To appear in: *J. of Supercritical Fluids*

Received date: 23-3-2016
Revised date: 29-6-2016
Accepted date: 30-6-2016



Please cite this article as: M. Wannassi, I. Raspo, Numerical study of non-isothermal adsorption of Naphthalene in supercritical CO₂: behavior near critical point, *The Journal of Supercritical Fluids* (2016), <http://dx.doi.org/10.1016/j.supflu.2016.06.020>

This is a PDF file of an unedited manuscript that has been accepted for publication. As a service to our customers we are providing this early version of the manuscript. The manuscript will undergo copyediting, typesetting, and review of the resulting proof before it is published in its final form. Please note that during the production process errors may be discovered which could affect the content, and all legal disclaimers that apply to the journal pertain.

1

2

3

Highlights

4

5 • Non-isothermal adsorption in near-critical binary mixtures was investigated by
6 numerical simulations.

7 • The adsorption behavior near solvent's critical point has been analyzed.

8 • The effect of divergent properties and the piston effect were highlighted.

9 • A strong dependence to temperature and pressure variations in the vicinity of the
10 critical point was depicted.

11

12

13

14

15

16

17

18

19

20

21

22

23

24 Numerical study of non-isothermal adsorption of Naphthalene
25 in supercritical CO₂ : behavior near critical point

26 Manel Wannassi*, Isabelle Raspo

27 Aix Marseille Univ, CNRS, Centrale Marseille, M2P2, Marseille, France

28

29

30

31 **Abstract**

32

33 In this study, adsorption in a model binary mixture is investigated near the critical point in a
34 side-heated cavity. The diverging behavior of the equilibrium constant and the Piston effect
35 are taken into account and their influence on the adsorption process is pointed to. The
36 modeling is based on numerical integration of the differential equations, considering the
37 Navier-Stokes equations coupled with the energy and mass diffusion balances. By means of
38 this model, the temperature, density and adsorbed concentration profiles are drawn at different
39 times. Some fundamental concepts about the system's response to the heating are illustrated.
40 The results reveal that the adsorption process is influenced by the combined effect of several
41 parameters, such as the gravity and the proximity to the critical point. In particular, the
42 adsorbed amount exhibits a reversed dependency on the wall heating very close to the critical
43 point, which confirms the complexity of such a process in binary systems near critical
44 conditions.

45 Keywords: Supercritical fluids; Adsorption; Piston effect; Numerical analysis

46

47 1. Introduction

48 The supercritical state was first reported in 1822 by Baron Gagniard de la Tour [1], but
49 only one hundred years later, supercritical techniques have received increased attention and
50 have been used in analytical and on an industrial scale. This state is achieved when the
51 temperature and the pressure of a substance is set over their critical values. So the properties

52 of a supercritical fluid range between those of a liquid and a gas and the distinction between
53 the liquid and the gas phases is not possible. Some of the properties of a supercritical fluid are
54 more liquid-like, whereas others are more gas-like.

55 Moreover, very close to the critical point, some properties diverge and others tend to
56 zero. In fact, a small raise in pressure remarkably increases the fluid density and this effect
57 diminishes with increasing distance from the critical point. On the other hand, a supercritical
58 fluid has a higher diffusion coefficient and lower viscosity and surface tension than a liquid
59 solvent, which leads to a more favorable mass transfer. Supercritical fluids exhibit very
60 interesting qualities with regard to their physicochemical properties as well as ecology and
61 economy. They are used as an alternative to organic liquid solvents in several applications
62 such as cleanings [2-4]. Adsorption technologies using supercritical fluids have been also
63 focused due to their potential applications including analytical extractions, activated carbon
64 regeneration and soil remediation. Several studies have investigated the supercritical
65 adsorption characteristics of many systems [5-12]. When adsorption is concerned,
66 thermodynamic and kinetic aspects should be involved to know more details about its
67 performance and mechanisms.

68 In the framework of isothermal supercritical adsorption, there have been numerous
69 publications in literature dealing with the modeling of adsorption equilibrium using the most
70 common adsorption isotherm models, i.e. the Langmuir, the Freundlich and the Redlich-
71 Peterson models [6-7, 13-16]. All the experimental conditions used correspond to
72 thermodynamic states relatively beyond the critical point because the adsorption equilibrium
73 is influenced by the system temperature, pressure and by the supercritical fluid properties in
74 the vicinity of the critical point. In contrast, supercritical adsorption systems close to the
75 solvent's critical point have received much less explicit attention in the open literature. The
76 experimental studies in this area are scarce. A thermodynamic analysis of near critical binary

77 mixtures was established by Afrane and Chimowitz [17]. The authors studied the adsorption
78 thermodynamics of dilute solutes adsorbing from high pressure supercritical fluid using the
79 Henry's law. However, set under high pressures, the results showed an extremely weak
80 dependence to pressure and to the composition of the supercritical solvent phase. In
81 chromatography, the proximity to the critical point was early reviewed by Van Wasen et al.
82 [20]. The authors pointed out the unusual behavior of equilibrium partition coefficients in the
83 near-critical region. Many other works also showed interesting features of data in this region
84 [21-22]; in particular, papers by Schmitz et al. [23] and Klesper and Schmitz [24] provided
85 striking evidence of the highly nonlinear behavior of equilibrium coefficients with respect to
86 pressure and temperature variations, as the critical point of the fluid phase is approached. We
87 believe that an adequate explanation of the thermodynamic basis of these phenomena in
88 adsorption process taking into account both temperature and pressure effects is necessary.
89 And it is also important to show the influence of the divergent character of thermodynamic
90 properties and transport coefficients in near-critical systems on adsorption system behavior.

91 This is precisely the aim of this paper. For this purpose, adsorption of a model solute
92 from supercritical CO₂ was investigated in a small side-heated cavity by means of 2D
93 numerical simulations. Naphthalene was chosen as a model solute because its phase equilibria
94 with CO₂ has been thoroughly studied [18-19]. There are extensive data available for this
95 system that have been confirmed. The first section of the paper is devoted to the mathematical
96 modeling of the problem and the numerical method used for the simulations. The modeling of
97 the adsorption reaction at the solid boundaries is exposed in details. Then, the effect of the
98 mass fraction and the proximity to the critical point are discussed for wide temperature and
99 pressure conditions. The results show a strong dependence to temperature and pressure
100 variations when the critical point is approached. We ended up with the effect of Damköhler
101 number on the adsorbed mass fraction.

102

103 2. Mathematical modeling

104 2.1 Problem under investigation

105 The problem we consider is that of a dilute solute (Naphthalene in this case, named
106 species 2) in supercritical CO₂ (named species 1). The physical properties of each pure
107 compound are given in Table 1. The Naphthalene-CO₂ mixture is enclosed in a square cavity
108 of height $H=1\text{mm}$ and subjected to the earth gravitational field g . The cavity vertical walls are
109 made of activated carbon (see Fig. 1). The activated carbon was chosen as a model adsorbent
110 for this problem allowing as considering an adsorption reaction at the solid-fluid interface.
111 Here, we emphasize that the chosen mixture as the adsorbent material is only generic since
112 the aim of this study is to qualitatively investigate the influence of the proximity to the critical
113 point on an adsorption reaction. Initially, the fluid is considered in thermodynamic
114 equilibrium at a constant temperature T_i slightly above the mixture critical temperature
115 $T_{cm} = 307.65\text{ K}$ such that $T_i = (1 + \varepsilon) T_{cm}$, where ε defines the dimensionless proximity to
116 the critical point ($\varepsilon \ll 1$), and the density is equal to the mixture critical density
117 $\rho_{cm} = 470\text{ kg}\cdot\text{m}^{-3}$. The critical properties, T_{cm} and ρ_{cm} correspond to the LCEP (“Lower
118 Critical EndPoint”) of the mixture and are slightly above the critical point of CO₂
119 ($T_{c1} = 304.21\text{ K}$, $\rho_{c1} = 467.8\text{ kg}\cdot\text{m}^{-3}$). A weak gradually heating is then applied at the solid
120 plate ($x=0$). The hot temperature is noted $T_h = T_i + \delta T$ where δT is about hundreds mK, while
121 maintaining the other side at its initial temperature T_i (noted T_{co}). An adiabatic boundary
122 condition was applied to the non-reactive walls.

123

124

125

126
127
128
129
130
131
132
133
134
135
136

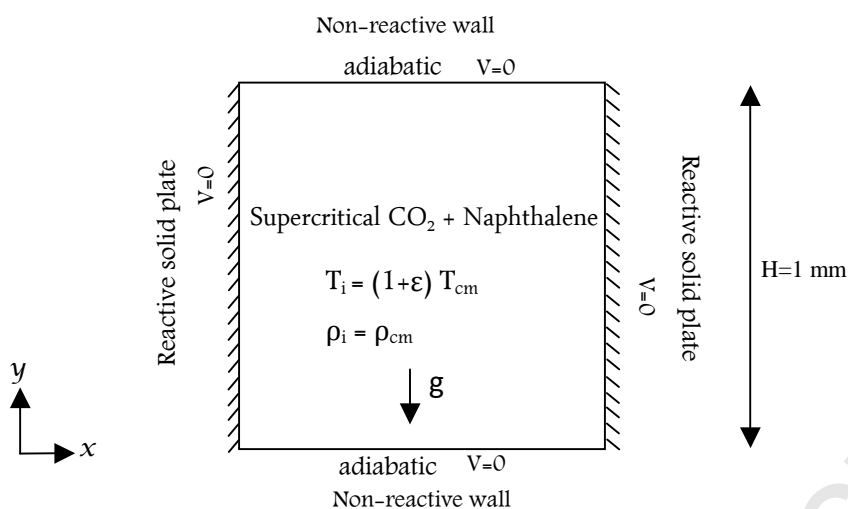


Fig. 1. Physical configuration

Table 1
Pure component properties

	T_c (K)	ρ_c (kg.m ⁻³)	P_c (bar)	M (kg.mol ⁻¹)	ω	v_b (cm ³ .mol ⁻¹)	E_a (J mol ⁻¹)
CO₂ (1)	304.21	467.8	73.8	$4.401 \cdot 10^{-2}$	0.225	-	-
Naphthalene (2)	748.40	314.9	40.5	$1.282 \cdot 10^{-1}$	0.302	155	101.4

137
138

139 2.2 Governing equations

140 The mathematical model is based on the 2D time-dependent and compressible Navier-
141 Stokes equations, coupled with energy and mass diffusion equations including the
142 supplemental Peng-Robinson equation of state. In order to reduce computational costs, a low
143 Mach number approximation is used [25]. This approximation is valid since Mach numbers
144 about 10^{-4} are obtained. Thus, the total pressure is split into two parts: a homogeneous
145 thermodynamic part $P_{th}(t)$, which appears in the equation of state and in the energy equation
146 and only depends on time t , and a non-homogeneous dynamic part $P_{dyn}(x, y, t)$, appearing in
147 the momentum equation and which varies with time and space. In this study, the dynamic
148 pressure is strongly smaller than the thermodynamic part. Consequently, the total pressure is
149 little different from the thermodynamic pressure and the evolution of P_{th} governs that of the

150 total pressure. In [38], a modification of the Low Mach number Approximation was proposed
 151 to account for the strong stratification of fluids near the critical point. We tested this
 152 modification and we noted that, for the present problem, the results obtained with and without
 153 the modification were the same. Therefore, the original approximation [25] was used for the
 154 simulations reported in this paper.

Table 2

Initial parameters

T_i (K)	ρ_i (kg.m ⁻³)	λ_i (W.m ⁻¹ .K ⁻¹)	C_{v_i} (J.kg ⁻¹ .K ⁻¹)	μ_i (Pa.s)	$(D_{21})_i$ (m ² .s ⁻¹)
307.75	470	0.098332532	1325.839	3.33828×10^{-5}	2.19525×10^{-8}
308.15	470	0.096196327	1306.27	3.34016×10^{-5}	2.19686×10^{-8}
309.15	470	0.091343811	1269.32	3.34485×10^{-5}	2.20090×10^{-8}
311.15	470	0.083368892	1214.86	3.35423×10^{-5}	2.20895×10^{-8}
318.15	470	0.066814297	1074.57	3.38700×10^{-5}	2.23679×10^{-8}

155

156 The dimensionless formulation was obtained using T_{cm} as characteristic temperature, ρ_i as
 157 characteristic density, $\rho_i (R / M_1) T_{cm}$ (with R is the perfect gas constant ($R=8.3145$ J mol⁻¹ K⁻¹)
 158 ¹) as characteristic pressure, H as characteristic length, the time scale of the piston effect as

159 characteristic time, $t_{PE} = \frac{t_d}{(\gamma_m - 1)^2}$, where t_d is the characteristic time of thermal diffusion,

160 γ_m the capacity ratio of the mixture (see Appendix A) and H/t_{PE} was taken as the

161 characteristic velocity. The transport properties such as the dynamic viscosity μ , the isochoric
 162 specific heat capacity C_v , the thermal conductivity λ and the diffusion coefficient D_{21} were

163 dimensionless, relative to their respective initial values $(\mu_i, \lambda_i, C_{v_i}, (D_{21})_i)$. Thus, the

164 governing equations in a dimensionless form are:

$$165 \quad \frac{\partial \rho}{\partial t} + \nabla \cdot (\rho \mathbf{V}) = 0 \quad (1)$$

$$166 \quad \rho \frac{\partial \mathbf{V}}{\partial t} + \rho \mathbf{V} \cdot \nabla \mathbf{V} = -\nabla P_{dyn} + \frac{1}{Re} \Delta \mathbf{V} + \frac{1}{3Re} \nabla (\nabla \cdot \mathbf{V}) + \frac{1}{Fr} \rho \quad (2)$$

$$\begin{aligned}
\rho \frac{\partial T}{\partial t} + \rho \mathbf{V} \cdot \nabla T &= - \frac{C_{v0}}{C_{vi}} (\gamma_0 - 1) \left[P_{th} - T \left(\frac{\partial P_{th}}{\partial T} \right)_{\rho w} \right] (\nabla \cdot \mathbf{V}) \\
167 \quad + \frac{\gamma}{\text{RePr}} \nabla \cdot (\lambda^* \nabla T) &- \left[(\bar{U}_2^* - \bar{U}_1^*) + \frac{C_{v0}}{C_{vi}} (\gamma_0 - 1) \left(P_{th} - T \left(\frac{\partial P_{th}}{\partial T} \right)_{\rho w} \right) (\bar{V}_2^* - \bar{V}_1^*) \right] \times \\
&\frac{1}{(\gamma - 1)^2 Le} \nabla \cdot (\rho D_{21}^* \nabla w)
\end{aligned} \tag{3}$$

$$168 \quad \rho \frac{\partial w}{\partial t} + \rho \mathbf{V} \cdot \nabla w = \frac{1}{(\gamma - 1)^2 Le} \nabla \cdot (\rho D_{21}^* \nabla w) \tag{4}$$

169 \mathbf{V} is the velocity of components u and v in the x - and y -directions respectively, w is the mass
170 fraction, γ is the ratio of the isobaric and isochoric specific heats calculated from the
171 equation of state (see Appendix A) with γ_0 and C_{v0} corresponding to the values for a perfect
172 gas ($\gamma_0 = 1.3$, $C_{v0} = 3R / M_1$). The value of C_{vi} for the initial state was taken from the NIST
173 (see Table 2). The dimensionless numbers are respectively, the Mach number Ma , the
174 Reynolds number Re , the Froude number Fr , the Prandtl number Pr and the Lewis number Le
175 and are defined as:

$$176 \quad Ma = \frac{V_{PE}}{c_0}, \quad Re = \frac{\rho_i V_{PE} H}{\mu_i}, \quad Fr = \frac{V_{PE}^2}{g H}, \quad Pr = \frac{\mu_i \gamma C_{vi}}{\lambda_i}, \quad Le = \frac{\lambda_i}{\rho_i \gamma C_{vi} (D_{21})_i}$$

177 where $c_0 = \sqrt{\gamma_0 (R / M_1) T_{cm}}$ is the sound speed and $V_{PE} = H / t_{PE}$ is the characteristic velocity

178 of the piston effect.

Table 3
Characteristic times (piston effect t_{PE} , thermal diffusion t_d , mass diffusion t_{Md} , adsorption t_{ad})

T_i (K)	t_{PE} (s)	t_d (s)	t_{Md} (s)	t_{ad} (s)
307.75	0.1999	115.6989	45.5530	45.5530 $\times 10^5$
308.15	0.2367	106.9022	45.5194	45.5194 $\times 10^5$
309.15	0.3333	91.1253	45.4359	45.4359 $\times 10^5$
311.15	0.5404	73.0746	45.2704	45.2704 $\times 10^5$
318.15	1.2621	49.2332	44.7069	44.7069 $\times 10^5$

179

180 In Eq. (3), \bar{U}_k^* and \bar{V}_k^* are respectively the dimensionless partial molar internal energy and
 181 partial molar volume expressed as follow:

$$182 \quad \bar{U}_k^* = \bar{U}_k / (M_2 C_{vi} T_{cm}) \quad \text{and} \quad \bar{V}_k^* = \bar{V}_k / (M_2 / \rho_i) \quad \text{for } k=1,2.$$

183 The expressions of \bar{U}_k and \bar{V}_k calculated using the Peng Robinson equation of state are
 184 given in Appendix B.

185 The following relationship is used for $\theta(w)$:

$$186 \quad \theta(w) = 1 - \left(1 - \frac{M_1}{M_2}\right) w$$

187 with M_1 and M_2 (kg mol^{-1}) are respectively, the molecular weight of CO_2 and Naphthalene
 188 (see Table 1).

189 The superscript (*) refers to dimensionless parameters.

190 For thermal conductivity λ ($\text{W.m}^{-1}.\text{K}^{-1}$), the following correlation is used [26]:

$$191 \quad \lambda(T, \rho) = \lambda_0(T) + \lambda_e(\rho) + \Delta\lambda_c(T, \rho),$$

192 The first term $\lambda_0(T)$ corresponds to the limit of small densities and is expressed as follow:

$$193 \quad \lambda_0(T) = -7.6683 \times 10^{-3} + 8.0321 \times 10^{-5} T$$

194 The second term $\lambda_e(\rho)$ is the excess property and is expressed as follow:

$$195 \quad \lambda_e(\rho) = 3.0990 \times 10^{-5} \rho + 5.5782 \times 10^{-8} \rho^2 + 2.5990 \times 10^{-17} \rho^5,$$

196 And the third term is the critical enhancement:

$$197 \quad \Delta\lambda_c(T, \rho) = \left(\frac{1.6735}{T - 291.4686} - 0.2774 + 7.4216 \times 10^{-4} T \right) \times \exp\left(-C^2 (\rho - \rho_{c1})^2\right)$$

198 with $\begin{cases} C = 6.7112 \times 10^{-3} & \text{if } \rho < \rho_{c1} \\ C = 6.9818 \times 10^{-3} & \text{if } \rho > \rho_{c1} \end{cases}$

199 The binary mass diffusion coefficient, D_{21} ($\text{m}^2 \text{s}^{-1}$), is calculated with the Wilke-Chang
200 equation [27]:

201
$$D_{21} = 7.4 \times 10^{-15} \frac{T \sqrt{\Phi 10^3 M_1}}{\mu v_{b2}^{0.6}},$$

202 with v_{b2} ($\text{cm}^3 \text{mol}^{-1}$) the molar volume of Naphthalene at boiling point, Φ the association
203 factor ($\Phi = 1$ for CO_2).

204 The thermodynamic state of the mixture is described by the Peng-Robinson equation of state
205 in the framework of the one-fluid theory. We can then compute the thermodynamic pressure
206 as follow:

207
$$P_{th} = \frac{T \rho \theta(w)}{1 - b^*(w) \rho / \theta(w)} - \frac{a^*(T, w) \rho^2}{1 + 2b^*(w) \rho / \theta(w) - b^*(w)^2 \rho^2 / \theta(w)^2} \quad (5)$$

208 Where:

209
$$a^*(T, w) = a_1^*(T) (1-w)^2 + 2a_{12}^*(T) w (1-w) + a_2^*(T) w^2,$$

210
$$b^*(w) = b_1^* (1-w)^2 + 2b_{12}^* w (1-w) + b_2^* w^2,$$

211
$$a_1^*(T) = 1.487422 \frac{T_{c1}}{T_{cm}} \frac{\rho_i}{\rho_{c1}} \left[1 + \beta_1 \left(1 - \sqrt{T (T_{cm} / T_{c1})} \right) \right]^2$$

212
$$a_2^*(T) = 1.487422 \frac{M_1 T_{c2}}{M_2 T_{cm}} \frac{\rho_i}{\rho_{c2}} \left[1 + \beta_2 \left(1 - \sqrt{T (T_{cm} / T_{c2})} \right) \right]^2$$

213
$$b_j^* = 0.253076 \left(\frac{\rho_i}{\rho_{cj}} \right) \text{ with } j=(1,2)$$

$$214 \quad a_{12}^*(T) = \sqrt{a_1^*(T)a_2^*(T)}(1 - k_{12}),$$

$$215 \quad b_{12}^* = \frac{1}{2} \left(b_1^* \frac{M_1}{M_2} + b_2^* \right) (1 - l_{12}),$$

$$216 \quad \beta_j = 0.37464 + 1.54226\omega_j - 0.26992\omega_j^2 \quad (j=1,2)$$

217 with ω the acentric factor (Table 1). The binary interaction parameters k_{12} and l_{12} are

218 determined so as to minimize the error between the calculated and experimental solubility
 219 data. These two parameters are temperature dependent and they are obtained through these
 220 formulae [28]:

$$221 \quad k_{12} = k'_{12} + k''_{12} \left(\frac{308.15}{T} - 1 \right),$$

$$222 \quad l_{12} = l'_{12} + l''_{12} \left(\frac{308.15}{T} - 1 \right)$$

223 The values of the binary interaction parameters predicted by a least square method are then:

$$224 \quad k'_{12} = 0.0395, \quad k''_{12} = 0.0114, \quad l'_{12} = -0.1136 \quad \text{and} \quad l''_{12} = -0.3103.$$

225

226 As it can be noted, the equations (1) – (5) are coupled for a given time step. This coupling
 227 can be reduced by using an explicit scheme to evaluate the convective terms in Eq. (3). But
 228 the energy source term involving $\nabla \cdot V$ must be implicitly evaluated because it accounts for
 229 the piston effect, namely the thermoacoustic effect responsible for fast heat transfer near the
 230 liquid-gas critical point. So in order to decouple the energy equation (Eq. (3)) and the Navier-

231 Stokes equations (Eqs. (1)- (2)), the velocity divergence, must be calculated using only the
 232 thermodynamic variables as explained by [29-30].

233 As part of the low Mach number approximation and for the dimensionless equations and if we
 234 consider the equation of state written in the general form $P_{th}=F(T, \rho, w)$, the total derivative
 235 of F with respect to time t leads to the relation:

236

$$237 \frac{dT}{dt} = \frac{-\left(\frac{\partial F}{\partial \rho}\right)_{T,w} \frac{d\rho}{dt} + \frac{dP_{th}}{dt} - \left(\frac{\partial F}{\partial w}\right)_{T,\rho} \frac{dw}{dt}}{\left(\frac{\partial F}{\partial T}\right)_{\rho,w}} \quad (6)$$

238 Moreover, the continuity equation (1) can also be written in the following form:

239

$$240 \frac{d\rho}{dt} = -\rho(\nabla \cdot \mathbf{V}) \quad (7)$$

241

242 Then, inserting Eq. (6) in the energy equation Eq. (3) using Eq. (7) for the computation of
 243 $d\rho/dt$ and Eq. (4) for the computation of dw/dt , lead finally to the following expression for the
 244 velocity divergence:

$$245 \nabla \cdot \mathbf{V} = \frac{\left\{ \rho \frac{dP_{th}}{dt} - \frac{\gamma}{\text{Re Pr}} \left(\frac{\partial F}{\partial T}\right)_{\rho,w} \nabla \cdot (\lambda^* \nabla T) - \left[\left(\frac{\partial F}{\partial w}\right)_{T,\rho} - \frac{1}{\theta(w)} A(\bar{U}^*, \bar{V}^*) \left(\frac{\partial F}{\partial T}\right)_{\rho,w} \right] \right\} \times \left[\frac{1}{(\gamma-1)^2 Le} \nabla \cdot (\rho D_{21}^* \nabla w) \right]}{1} \quad (8)$$

$$\frac{C_{v,0}}{C_{v,i}} (\gamma_0 - 1) \left(\frac{\partial F}{\partial T}\right)_{\rho,w} \left(P_{th} - T \left(\frac{\partial P_{th}}{\partial T}\right)_{\rho,w} \right) - \rho^2 \left(\frac{\partial F}{\partial \rho}\right)_{T,w}}$$

246 with $A(\bar{U}^*, \bar{V}^*) = (\bar{U}_2^* - \bar{U}_1^*) + \frac{C_{v,0}}{C_{v,i}} (\gamma_0 - 1) \left[P_{th} - T \left(\frac{\partial P_{th}}{\partial T}\right)_{\rho,w} \right] \times (\bar{V}_2^* - \bar{V}_1^*)$

247 The expressions of $\left(\frac{\partial F}{\partial T}\right)_{\rho,w}$, $\left(\frac{\partial F}{\partial w}\right)_{T,\rho}$ and $\left(\frac{\partial F}{\partial \rho}\right)_{T,w}$ are reported in Appendix C.

248 Thanks to Eq. (8), we are now able to solve the governing equations in two uncoupled
 249 steps, namely the energy equation and the equation of state on the one hand and the Navier-
 250 Stokes equations on the other hand. The algorithm is detailed in section 2.4.

251 In this study, only the gravity effect was considered, the stratification of the fluid was not
 252 taken into account, because we have tested several cases with stratification and no effect was
 253 observed.

254 The initial and boundary conditions in dimensionless form are:

255 *CI: $t = 0$*

$$T_i = 1 + \varepsilon$$

$$\rho_i = 1$$

256 w_i fixed

$$P_i = \frac{(1 + \varepsilon)\theta(w_i)}{1 - b^*(w_i)/\theta(w_i)} - \frac{a^*(1 + \varepsilon, w_i)}{1 + 2b^*(w_i)/\theta(w_i) - b^*(w_i)^2/\theta(w_i)^2}$$

257 *BC:*

258 *No-slip walls* were considered so $u = v = 0$ at the two plates.

259 *At $x=0$* $T_h = 1 + \varepsilon + \delta T^*$

260 with $\delta T^* = \delta T / T_{cm}$

261 *At $x=l$* $T_{co} = 1 + \varepsilon$

262 *At $y=0, l$* $\frac{\partial T}{\partial y} = 0$ (adiabatic walls)

263

264 *2.3 Modeling of the adsorption reaction*

265 At the interfaces $x=0$ and H , an adsorption reaction of Naphthalene on activated
 266 carbon is considered. The choice of such adsorption system can be explained by the extensive
 267 use of activated carbon as new-type high-efficiency adsorbent due to its high adsorption
 268 capacities and high mass transfer rates. However, the model description can be applied to any
 269 other adsorption system. The main objective here is to see how a supercritical mixture
 270 behaves in the vicinity of reactive wall. So, we will focus essentially on the fluid side rather
 271 than on what happens in the solid itself.

272 The species diffusion equation, (Eq. (4)), can be written in this form:

$$273 \quad \rho \frac{\partial w}{\partial t} + \rho u \frac{\partial w}{\partial x} + \rho v \frac{\partial w}{\partial y} = \nabla \cdot (\rho D_{21} \nabla w)$$

274 where u and v are the velocity of components in the x - and y -directions respectively.

275 The boundary conditions are:

276 *At the horizontal non-reactive walls*

$$277 \quad \frac{\partial w}{\partial y} = 0 \quad \text{for } y=0 \text{ and } y=H$$

278 *At the vertical reactive walls*, a first order kinetic adsorption model is used:

$$279 \quad D_{21} \frac{\partial w}{\partial n} = K_a w$$

280 where n is the normal to the surface at $x=0$ and $x=H$ and $K_a = k_a / S_{ac}$ with k_a the adsorption rate
 281 constant ($\text{m}^3 \cdot \text{kg}^{-1} \cdot \text{s}^{-1}$) and S_{ac} the specific surface area of activated carbon ($\text{m}^2 \cdot \text{kg}^{-1}$).

282 Assuming small variations of temperature and pressure, K_a can be approximated by the first-
 283 order term of its Taylor series in the vicinity of (T_i, P_i) :

$$284 \quad K_a = K_a(T_i, P_i) + \left(\frac{\partial K_a}{\partial T} \right)_P (T - T_i) + \left(\frac{\partial K_a}{\partial P} \right)_T (P - P_i) \quad (9)$$

285 The adsorption rate constant k_a can be computed by $k_a = K_2 \cdot k_d$ where K_2 is the adsorption
 286 equilibrium constant ($\text{m}^3 \cdot \text{kg}^{-1}$) and k_d is the desorption rate constant obtained through the
 287 Arrhenius law:

$$288 \quad k_d = A \exp\left(-\frac{E_a}{RT}\right)$$

289 with E_a the activation energy and A the pre-exponential factor of Arrhenius.

290 The first term of Eq. (9) can be then considered as:

$$291 \quad K_{ai} = K_a(T_i, P_i) = \frac{k_d(T_i) K_2(T_i, P_i)}{S_{ac}}$$

292 The partial derivatives of K_a with respect to temperature and pressure are written as follow:

$$293 \quad \left(\frac{\partial K_a}{\partial T}\right)_p = \frac{1}{S_{ac}} \left(\frac{\partial k_a}{\partial T}\right)_p = \frac{k_d(T_i) K_2(T_i, P_i)}{S_{ac}} \left[\frac{E_a}{RT^2} + \left(\frac{\partial \ln K_2}{\partial T}\right)_p \right]$$

$$294 \quad \left(\frac{\partial K_a}{\partial P}\right)_T = \frac{1}{S_{ac}} \left(\frac{\partial k_a}{\partial P}\right)_T = \frac{k_d(T_i) K_2(T_i, P_i)}{S_{ac}} \left(\frac{\partial \ln K_2}{\partial P}\right)_T$$

295 Thus Eq. (9) becomes:

$$296 \quad K_a(T, P) = K_{ai} \left\{ 1 + \left[\frac{E_a}{RT^2} + \left(\frac{\partial \ln K_2}{\partial T}\right)_p(T_i, P_i) \right] (T - T_i) + \left(\frac{\partial \ln K_2}{\partial P}\right)_T(T_i, P_i) (P - P_i) \right\} \quad (10)$$

297 The partial derivatives of K_2 with respect to temperature and pressure are obtained by
 298 equating differentials of the logarithm of the solute fugacity in the fluid and solid phases
 299 [31]:

$$300 \quad \left(\frac{\partial \ln K_2}{\partial T}\right)_p = \frac{\left(h_2^{IG} - \bar{h}_2^m\right) + \Delta H_2^{ads}}{RT^2} + \alpha^m \quad (11)$$

$$301 \quad \left(\frac{\partial \ln K_2}{\partial P} \right)_T = \frac{\bar{v}_2^{\infty,m}}{RT} - \kappa^m \quad (12)$$

302 where $\Delta H_2^{ads} = \bar{h}_2^s - h_2^{IG}$ is the heat of adsorption of the solute on the solid plate, \bar{h}_2^m and
 303 \bar{h}_2^s are the infinite-dilution partial molar enthalpies of solute in the mobile and stationary
 304 phases, respectively, h_2^{IG} is the enthalpy of the solute in the ideal gas state, $\bar{v}_2^{\infty,m}$ is the infinite-
 305 dilution partial molar volume of the solute in mobile phase and α^m, κ^m are respectively, the
 306 volume expansivity and the isothermal compressibility.

307 The infinite-dilution residual partial molar enthalpy ($h_2^{IG} - \bar{h}_2^m$) of the solute, α^m, κ^m and
 308 $\bar{v}_2^{\infty,m}$ are obtained using the Peng-Robinson equation of state and they are reported in
 309 Appendix D.

310 As shown by Eq. (10), the derivatives of the equilibrium adsorption constant, K_2 , with respect
 311 to temperature and pressure are directly involved in the definition of the boundary condition
 312 at the solid-fluid interface. So, it is important to assess the effect of temperature and pressure
 313 on these derivatives. A strong sensitivity to temperature and pressure can be guessed from
 314 Eqs. (11) – (12) since the infinite-dilution residual partial molar enthalpy, ($h_2^{IG} - \bar{h}_2^m$), the
 315 infinite dilution partial molar volume of the solute, $\bar{v}_2^{\infty,m}$, the isothermal compressibility, κ^m ,
 316 and the volume expansivity, α^m , diverge near the solvent critical point. This assumption is
 317 confirmed by Fig. 2 which shows the K_2 derivative profiles as a function of pressure for
 318 different temperatures. The profiles show a sharp minimum which becomes more important
 319 when the critical temperature is approached. Then this minimum is shifted to the high
 320 pressure domain and becomes less significant away from the critical point especially for
 321 $T=318.15$ K. In this region (high pressure domain), the effect of the temperature on the
 322 isothermal derivative is less pronounced. In the same way, the isobaric derivative of the

323 equilibrium constant as a function of temperature is shown in Fig. 3 for different pressures.
 324 For pressures close to the critical one, namely $P \leq 8.909$ MPa, a divergence of the derivative is
 325 observed as the critical temperature is approached. Then, from 9 MPa, a behavior change can
 326 be depicted with the appearance of a maximum which decreases and is shifted to the high
 327 temperature domain when the pressure increases. One can also notice a similar trend for high
 328 pressures and high temperatures. Therefore beyond the critical point the effect of the pressure
 329 and temperature is no longer noticed.

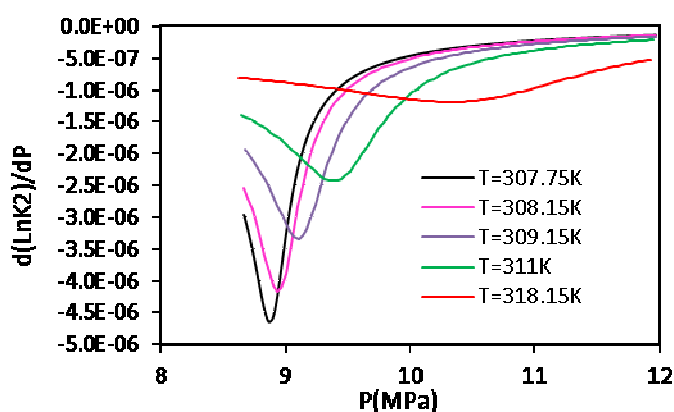


Fig. 2. Equilibrium constant derivative vs. pressure

330

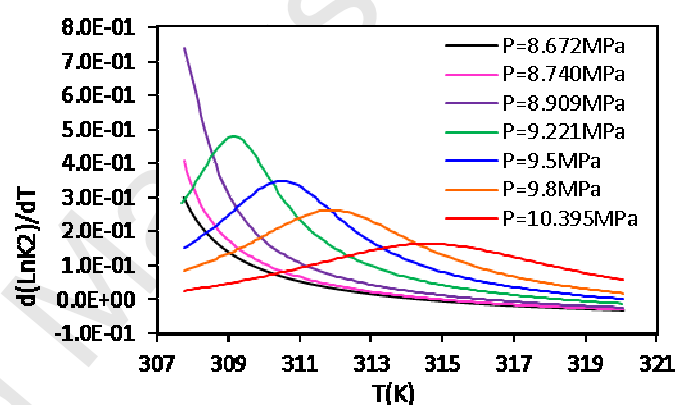


Fig 3. Equilibrium constant derivative vs. temperature

331 For this reason, a particular attention was paid to the effects of temperature and pressure on
 332 the equilibrium adsorption constant in this study because a wide range of temperature and
 333 pressure were considered. Moreover, changes near and far from the critical point will help us
 334 to explain our results later.

336 It must be noted that the divergence of the infinite-dilution properties (residual partial molar
 337 enthalpy and partial molar volume) of the solute is not specific of Naphthalene but it is a
 338 universal behavior for dilute mixtures [32-33]. Therefore, the results obtained in this paper for
 339 Naphthalene in supercritical CO_2 are likely to be observed in all dilute binary mixtures, at
 340 least on a qualitative point of view. Moreover, the nature of the adsorbent material appears

341 only through the heat of adsorption, ΔH_2^{ads} , in Eq. (11), and therefore just for the variation of
 342 K_2 with respect to temperature. We compared the evolutions of $d(\text{Ln}K_2)/dT$ for soil ($\Delta H_2^{ads} =$
 343 -46054.8 J/mol) and for activated carbon ($\Delta H_2^{ads} = -83736 \text{ J/mol}$) as adsorbent material. The
 344 same variations were observed in both cases with maxima occurring for the same
 345 temperatures but with slightly different values: for example, the maximum for $P = 9.221 \text{ MPa}$
 346 was equal to 0.52383 K^{-1} for soil and 0.47643 K^{-1} for activated carbon. These identical
 347 variations can be explained by the fact that the evolution of $d(\text{Ln}K_2)/dT$ is governed by the
 348 very large values of the infinite-dilution residual partial molar enthalpy, $(h_2^{IG} - \bar{h}_2^m)$, and of
 349 the volume expansivity, α^m , near the critical point. And these two properties are completely
 350 independent of the characteristics of the adsorbent material. Consequently, the results
 351 presented in this paper for adsorption on activated carbon are also relevant for any other
 352 adsorbent material.

353 In the framework of the Low Mach number approximation, the boundary condition for the
 354 mass fraction w on $x=0$ and H can then be expressed as:

$$355 \quad D_{21} \frac{\partial w}{\partial n} = K_{ai} D_k (T, P_{th}) w$$

$$356 \quad \text{with } D_k (T, P_{th}) = 1 + \left[\frac{E_a}{RT^2} + \left(\frac{\partial \text{Ln}K_2}{\partial T} \right)_P (T_i, P_i) \right] (T - T_i) + \left(\frac{\partial \text{Ln}K_2}{\partial P} \right)_T (T_i, P_i) (P - P_i)$$

357 In the dimensionless form, it will be written as:

$$358 \quad -\frac{D_{21}^*}{Da} \frac{1}{D_k} \frac{\partial w^*}{\partial n} = 1 - w^* \quad (13)$$

359 with $D_{21}^* = D_{21} / (D_{21})_i$, $w^* = (w - w_i) / w_i$ and Da is the Damköhler number defined as the
 360 ratio of the characteristic fluidic time scale (diffusion characteristic time) and chemical time
 361 scale (adsorption characteristic time):

$$362 \quad Da = \frac{HK_{ai}}{(D_{21})_i}$$

363 Eq. (13) leads to two Robin-type boundary conditions at $x=0$ and $x=1$:

$$364 \quad \text{At } x=0 \quad w^* + \frac{D_{21}^*}{Da} \frac{1}{D_k} \frac{\partial w^*}{\partial x} = 1 \quad (14)$$

365 At $x=1$, the wall is maintained at the initial temperature, thus, $D_{21}^*=1$:

$$366 \quad w^* - \frac{1}{Da} \frac{1}{D_k} \frac{\partial w^*}{\partial x} = 1 \quad (15)$$

367 2.4 Numerical method

368 The numerical integration of the model equations has been carried out using a second
 369 order semi-implicit scheme [34]: the convective terms are evaluated by an Adams-Bashforth
 370 scheme, and then the time integration of the resulting differential equations has been done
 371 with an implicit second order backward Euler scheme. The space approximation is performed
 372 using the Chebyshev-collocation method with Gauss-Lobatto points. For the computation of
 373 the convective terms, the derivatives are calculated in the spectral space and the products are
 374 performed in the physical one; the connection between the spectral and the physical spaces is
 375 realized through a FFT algorithm. On the other hand, the spectral differentiation matrices are
 376 used for the derivatives in the diffusive terms.

377 The computation of the velocity divergence by Eq. (8) allowed a decoupling between the
 378 thermodynamic variables T , ρ , P_{th} , w^* and that of the dynamic field. Consequently, the
 379 discretized equations can be solved in two successive steps: first, the thermodynamic
 380 variables are computed through the algorithm proposed by Ouazzani and Garrabos [29] and

381 then the Navier-Stokes equations are solved using the modified projection method developed
382 in [35] and extended to variable density flows. These two steps are detailed bellow.

383 2.4.1 Computation of the thermodynamic variables (T, ρ, P_{th}, w^*)

384

385 The discretised energy and diffusion equations can be written as Helmholtz equations with
386 time-dependent coefficients. In order to solve them using the diagonalization technique
387 developed in [36] for Helmholtz equations with constant coefficients, the density and the
388 transport coefficients λ^* and D_{21}^* are split into a constant part equal to the initial value and a
389 time-dependent part:

$$390 \alpha^{n+1} = 1 + (\alpha^{n+1} - 1) \text{ for } \alpha = \rho, \lambda^*, D_{21}^*$$

391 So, the discretized energy equation for example obtained as Helmholtz equation with constant
392 coefficients is written as follow:

$$393 \begin{aligned} \frac{\gamma}{\text{Re Pr}} \Delta T^{n+1} - \frac{3}{2\delta t} T^{n+1} &= \frac{3}{2\delta t} (\rho^{n+1} - 1) T^{n+1} - \frac{\gamma}{\text{Re Pr}} \nabla \cdot ((\lambda^{*n+1} - 1) \nabla T^{n+1}) \\ &+ \rho^{n+1} \left(\frac{-4T^n + T^{n-1}}{2\delta t} \right) + AB(\rho \mathbf{V} \cdot \nabla T)^{n,n-1} \\ &+ \frac{C_{v,0}}{C_{v,i}} (\gamma_0 - 1) \left[P_{th}^{n+1} - T^{n+1} \left(\frac{\partial P_{th}}{\partial T} \right)_{\rho,w}^{n+1} \right] (\nabla \cdot \mathbf{V})^{n+1} \\ &- \frac{w_i}{\theta(w^{n+1})} A \left(\bar{U}^{*n+1}, \bar{V}^{*n+1} \right) \frac{1}{(\gamma-1)^2 Le} \nabla \cdot (\rho^{n+1} D_{21}^{*n+1} \nabla w^{*n+1}) \end{aligned} \quad (16)$$

394 where δt is the time-step and the notation $AB(\cdot)$ means an Adams-Bashforth evaluation of the
395 quantity:

$$396 AB(\phi)^{n,n-1} = 2\phi^n - \phi^{n-1}.$$

397 The diagonalization process of the Helmholtz operator with constant coefficients is executed
398 only once in a preprocessing stage. After that, at each time step, the solution of Eq. (16) is
399 reduced to matrix products, leading to a very efficient solution technique.

400 Thus, the solution of the energy Eq. (16), the diffusion equation and the equation of state
401 is performed through the following iterative algorithm:

402 1. The variables T^{k-1} , P_{th}^{k-1} , ρ^{k-1} , $w^{*(k-1)}$ and $(\nabla \cdot V)_T^{k-1}$ are initialized at their values at the
403 previous time step n ;

404 2. The temperature T^k is obtained by the solution of the Helmholtz equation:

405

$$\begin{aligned} \frac{\gamma}{\text{Re Pr}} \Delta T^k - \frac{3}{2\delta t} T^k &= \frac{3}{2\delta t} (\rho^{k-1} - 1) T^{k-1} - \frac{\gamma}{\text{Re Pr}} \nabla \cdot ((\lambda^{k-1} - 1) \nabla T^{k-1}) \\ &+ \rho^{k-1} \left(\frac{-4T^n + T^{n-1}}{2\delta t} \right) + AB (\rho \mathbf{V} \cdot \nabla T)^{n,n-1} \\ &+ \frac{C_{v0}}{C_{vi}} (\gamma_0 - 1) \left[P_{th}^{k-1} - T^{k-1} \left(\frac{\partial P_{th}}{\partial T} \right)_{\rho,w}^{k-1} \right] (\nabla \cdot V)^{k-1} \\ &- \frac{w_i}{\theta(w^{k-1})} A \left(\bar{U}^{*k-1}, \bar{V}^{*k-1} \right) \frac{1}{(\gamma-1)^2 Le} \nabla \cdot (\rho^{k-1} D_{21}^{*k-1} \nabla w^{*k-1}) \end{aligned}$$

406

407 3. The mass fraction w^{*k} is obtained by the solution of the Helmholtz equation:

408

$$\begin{aligned} \frac{1}{(\gamma-1)^2 Le} \Delta w^{*k} - \frac{3}{2\delta t} w^{*k} &= \frac{3}{2\delta t} (\rho^{k-1} - 1) w^{*k-1} - \frac{1}{(\gamma-1)^2 Le} \nabla \cdot ((\rho^{k-1} D_{21}^{*k-1} - 1) \nabla w^{*k-1}) \\ &+ \rho^{k-1} \left(\frac{-4w^{*n} + w^{*n-1}}{2\delta t} \right) + AB (\rho V \cdot \nabla w^*)^{n,n-1} \end{aligned}$$

409

410 with the following Robin boundary conditions on adsorbing walls:

411

$$412 \quad w^{*k} + \frac{1}{Da} \frac{\partial w^{*k}}{\partial x} = 1 + \left(\frac{1}{Da} - \frac{D_{21}^{*k-1}}{Da} \frac{1}{D_k^{k-1}} \right) \frac{\partial w^{*(k-1)}}{\partial x} \quad \text{for } x=0$$

$$413 \quad w^{*k} - \frac{1}{Da} \frac{\partial w^{*k}}{\partial x} = 1 - \frac{1}{Da} \left(1 - \frac{1}{D_k^{k-1}} \right) \frac{\partial w^{*(k-1)}}{\partial x} \quad \text{for } x=1$$

414 4. The couple (P_{th}^k, ρ^k) is computed from the constraint of global mass conservation and the
415 equation of state. This computation must be performed through an iterative process;

416 5. The thermal conductivity λ^{*k} and the diffusion coefficient D_{21}^{*k} are updated.

417 6. The velocity divergence $(\nabla \cdot \mathbf{V})_T^k$ is computed by Eq. (8).

418 The steps 2 to 6 are repeated until convergence is achieved on temperature, thermodynamic
 419 pressure, density and mass fraction. The convergence criterion used is $\text{Max}(Res_T, Res_\rho, Res_w,$
 420 $Res_{P_{th}}) < 10^{-11}$, with $Res = \text{Max}((\phi^k - \phi^{k-1}) / \phi^{k-1})$ for $\phi = T, \rho, w, P_{th}$, and the maximum number of
 421 iterations is fixed to 250.

422

423 2.4.2 Solution of the Navier-Stokes equations

424

425 The second step is the solution of the Navier-Stokes equations. At the current time step
 426 $(n+1)$, temperature, density and velocity divergence are known. A projection-type algorithm
 427 such as those developed for the solution of incompressible Navier-Stokes equations can then
 428 be used. In the present work, the original projection method of Hugues and
 429 Randriamampianina [35] was modified to account for variable density flows [30, 39]. The
 430 advantage of this method compared to other projection methods is that it allows improving the
 431 accuracy on pressure and reducing the slip velocity. It consists in solving the Navier-Stokes
 432 equations by three successive steps.

433 1st Step: Computation of a preliminary pressure

434 The preliminary pressure \bar{P}_{dyn}^{n+1} is computed from a Poisson equation, derived from the
 435 discretized momentum equation, with Neumann boundary conditions obtained by the normal
 436 projection of the momentum equation on the boundary:

437

$$\begin{cases}
\Delta \bar{P}_{dyn}^{n+1} = \nabla \cdot \left[-AB (\rho \mathbf{V} \cdot \nabla \mathbf{V})^{n,n-1} + \rho^{n+1} \left(\frac{4\mathbf{V}^n - \mathbf{V}^{n-1}}{2\delta t} \right) + \frac{1}{Fr} \rho^{n+1} g \right] & \text{in } \Omega \\
+ \frac{4}{3Re} \Delta (\nabla \cdot \mathbf{V})_T^{n+1} + \frac{3}{2\delta t} \left(\frac{3\rho^{n+1} - 4\rho^n + \rho^{n-1}}{2\delta t} \right) & \\
\frac{\partial \bar{P}_{dyn}^{n+1}}{\partial n} = n \cdot \left[-AB (\rho \mathbf{V} \cdot \nabla \mathbf{V})^{n,n-1} - \rho^{n+1} \left(\frac{3\mathbf{V}_B^{n+1} - 4\mathbf{V}^n + \mathbf{V}^{n-1}}{2\delta t} \right) + \frac{1}{Fr} \rho^{n+1} g \right] & \text{on } \partial\Omega \\
+ \frac{4}{3Re} \nabla (\nabla \cdot \mathbf{V})_T^{n+1} - \frac{1}{Re} AB (\nabla \times (\nabla \times \mathbf{V}))^{n,n-1} &
\end{cases} \quad (17)$$

439

440 with Ω the computational domain ($\Omega =]-1,+1[\times]-1,+1[$), $\partial\Omega$ its boundary, \mathbf{V}_B^{n+1} the boundary
441 conditions of the velocity \mathbf{V}^{n+1} , $\partial/\partial n$ the normal derivative and $\nabla \cdot \mathbf{V}$ is calculated from
442 thermodynamic variables and noted $(\nabla \cdot \mathbf{V})_T$.

443 In Eq. (17), the term $\Delta \mathbf{V}^{n+1}$ was decomposed in the boundary condition using the formula:

444

$$445 \Delta \mathbf{V}^{n+1} = \nabla (\nabla \cdot \mathbf{V}^{n+1}) - \nabla \times (\nabla \times \mathbf{V}^{n+1})$$

446

447 and the rotational term was evaluated using an Adams-Bashforth scheme.

448

449 2nd Step: Computation of a predicted velocity \mathbf{V}^*

450

451 The predicted velocity field \mathbf{V}^* is computed implicitly from the momentum equation with
452 the gradient of the preliminary pressure instead of that of the actual pressure P_{dyn}^{n+1} . The
453 predicted velocity therefore satisfies the following problem:

454

$$\begin{cases}
\rho^{n+1} \frac{3\mathbf{V}^* - 4\mathbf{V}^n + \mathbf{V}^{n-1}}{2\delta t} + AB (\rho \mathbf{V} \cdot \nabla \mathbf{V})^{n,n-1} = -\nabla \bar{P}_{dyn}^{n+1} + \frac{1}{Re} \Delta \mathbf{V}^* + \frac{1}{3Re} \nabla (\nabla \cdot \mathbf{V})_T^{n+1} + \frac{1}{Fr} \rho^{n+1} g & \text{in } \Omega \\
\mathbf{V}^* = \mathbf{V}_B^{n+1} & \text{on } \partial\Omega
\end{cases} \quad (18)$$

456

457

458 Here again, we have to solve Helmholtz equations with variable coefficients for each
 459 velocity component. As for energy and mass diffusion equations, the density ρ^{n+1} is split into
 460 a constant part and a time-dependent part and the following Helmholtz equation with constant
 461 coefficient is solved iteratively:

$$\begin{aligned}
 \frac{1}{\text{Re}} \Delta \mathbf{V}^{*,l} - \frac{3}{2\delta t} \rho_0 \mathbf{V}^{*,l} &= \frac{3}{2\delta t} (\rho^{n+1} - \rho_0) \mathbf{V}^{*,l-1} + \nabla \bar{P}_{dyn}^{n+1} \\
 -\rho^{n+1} \left(\frac{4\mathbf{V}^n - \mathbf{V}^{n-1}}{2\delta t} \right) &+ AB (\rho \mathbf{V} \cdot \nabla \mathbf{V})^{n,n-1} \\
 -\frac{1}{3\text{Re}} \nabla (\nabla \cdot \mathbf{V})_T^{n+1} - \frac{1}{Fr} \rho^{n+1} \mathbf{g} &
 \end{aligned} \quad (19)$$

463
 464 The convergence is achieved when $\text{Max}(Res_u, Res_v) < 10^{-13}$, with $Res = \text{Max}((\cdot - \cdot^{l-1}) / \cdot^{l-1})$ for
 465 $= u, v$. Only 3 or 4 iterations are necessary.

466
 467 3rd Step: Correction step

468 The converged velocity field \mathbf{V}^* is then corrected by taking into account the pressure
 469 gradient at the current time step ($n+1$) so that the final velocity field satisfies the continuity
 470 equation:

$$\begin{cases}
 \frac{3}{2\delta t} (\rho^{n+1} \mathbf{V}^{n+1} - \rho^{n+1} \mathbf{V}^*) = -\nabla (P_{dyn}^{n+1} - \bar{P}_{dyn}^{n+1}) & \text{in } \Omega \cup \partial\Omega \\
 \mathbf{V}^{n+1} \cdot \mathbf{n} = \mathbf{V}_B^{n+1} \cdot \mathbf{n} & \text{on } \partial\Omega \\
 \frac{3\rho^{n+1} - 4\rho^n + \rho^{n-1}}{2\delta t} + \nabla \cdot (\rho^{n+1} \mathbf{V}^{n+1}) = 0 & \text{in } \Omega
 \end{cases} \quad (20)$$

473
 474 This system is solved through the following Poisson problem for the intermediate
 475 variable $\varphi = 2\delta t (P_{dyn}^{n+1} - \bar{P}_{dyn}^{n+1}) / 3$:

476

$$\begin{cases} \Delta \varphi = \nabla \cdot (\rho^{n+1} \mathbf{V}^*) + \frac{3\rho^{n+1} - 4\rho^n + \rho^{n-1}}{2\delta t} & \text{in } \Omega \\ \frac{\partial \varphi}{\partial n} = 0 & \text{on } \partial\Omega \end{cases} \quad (21)$$

478

479 The actual velocity field and pressure at the current time step ($n+1$) are finally calculated in480 $\Omega \cup \partial\Omega$ by the formulae:

$$481 \quad \mathbf{V}^{n+1} = \mathbf{V}^* - \frac{1}{\rho^{n+1}} \nabla \varphi \quad (22)$$

$$482 \quad P_{dyn}^{n+1} = \bar{P}_{dyn}^{n+1} + \frac{3}{2\delta t} \varphi \quad (23)$$

483

484

485

486

487

488

489

490

491

492

493

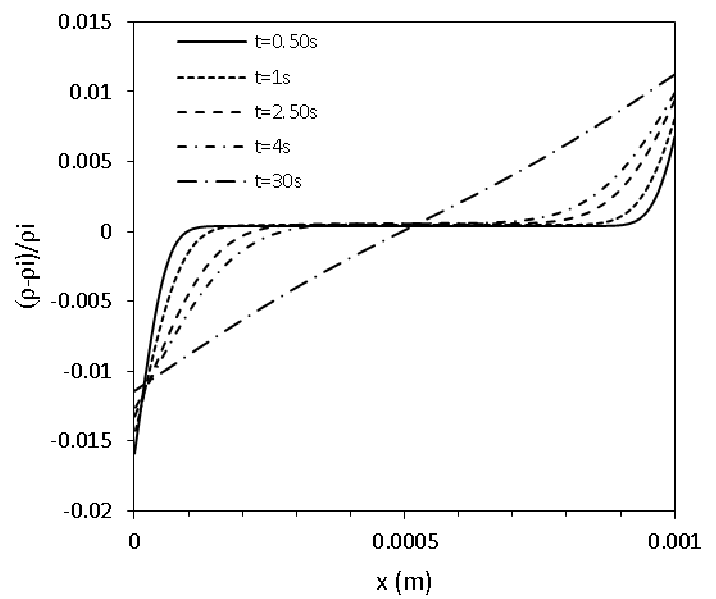
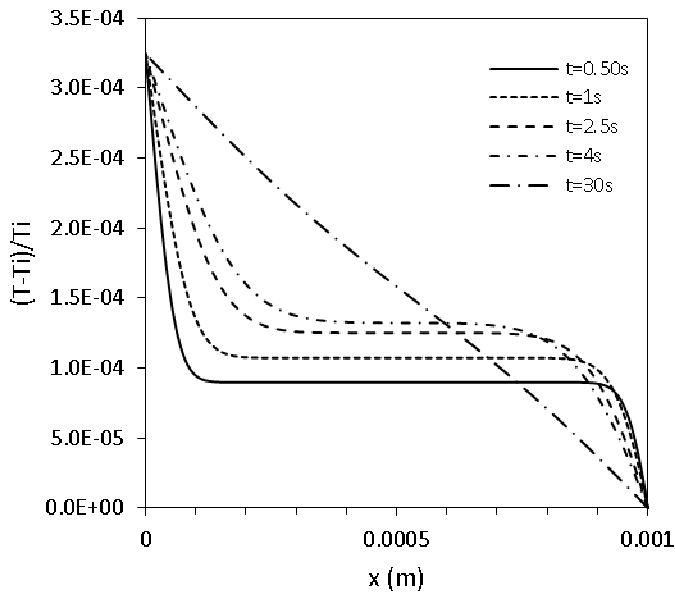
494

495

496

497

498 3. Results and discussions



499

500

501 Fig. 4. Profiles of the temperature perturbation at several
502 times for $T_i=308.15$ K and $\Delta T=100$ mK in the case $g=0$

503

504

505 Fig. 5. Profiles of the density perturbation at several
506 times for $T_i=308.15$ K and $\Delta T=100$ mK

507

508

509

510

511

512

513

514

515

516

517

518

519

520

521

522

523

524

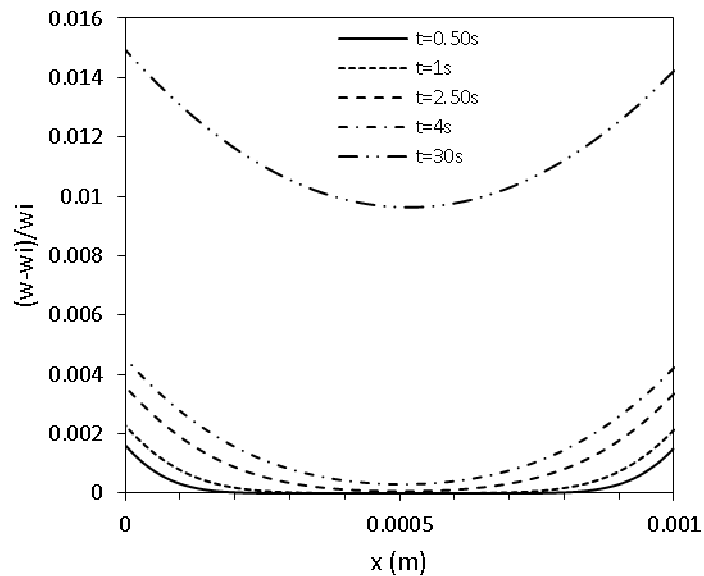
525

526

527

528

529

530 Fig. 6. Profiles of the mass fraction perturbation at several
531 times for $T_i=308.15$ K and $\Delta T=100$ mK in the case $g=0$

530 The system's response to the heating of the left vertical wall is explained in this

531 section. The analysis below is based on simulations carried out at various initial temperatures

532 T_i ranging from 307.75 K to 318.15 K and which correspond to dimensionless distances ϵ to
 533 the critical point ranging from 3.25×10^{-4} to 3.41×10^{-2} . The values of the different
 534 characteristic times of the problem are given in Table 3. It can be noted that, as the critical
 535 temperature is approached, the thermal diffusion and mass diffusion times strongly increase
 536 whereas the characteristic time of piston effect decreases. For all the simulations, the left side
 537 of the cavity (at $x=0$) is gradually heated following a cosine law expressed as:

$$538 \quad \delta T(t) = \begin{cases} 0.5 \Delta T \left(1 - \cos \left(\pi \frac{t}{t_{\text{heat}}} \right) \right) & \text{if } t \leq t_{\text{heat}} \\ \Delta T & \text{if } t \geq t_{\text{heat}} \end{cases}$$

539 where ΔT is the temperature increase and t_{heat} is the heating phase time corresponding to 200
 540 time steps. The influence of ΔT will be discussed later for different cases ($\Delta T = 50, 100, 150$
 541 and 200 mK).

542 3.1 General description

543 In the first part, the case of $T_i = 308.15$ K and $\Delta T = 100$ mK, is discussed. The
 544 Damköhler number is fixed to $Da = 10^{-5}$ and the initial mass fraction w_i corresponds to the
 545 solubility of Naphthalene in CO_2 .

546 The evolution of temperature and density distributions between the walls and at the cavity
 547 mid-height are illustrated in Figs. 4 and 5 for several times ($t = 0.5$ s, 1 s, 2.5 s, 4 s and 30 s)
 548 in the absence of gravity. Because of the very small thermal diffusivity near the critical point,
 549 the heating of the wall causes ultra-thin boundary layers at the wall-fluid interface. Due to the
 550 high isothermal compressibility, the fluid close to the heated side expands upward and
 551 converts some of the kinetic energy into thermal energy. This results in compressing
 552 adiabatically the rest of the fluid and leading to a quick increase of the thermodynamic
 553 pressure which induces a fast and homogeneous heating of the cavity bulk by thermo-acoustic

554 effects (piston effect). During the heating phase, temperature, and therefore density, at the
555 heated wall change at each time step and, as a consequence, temperature and density gradients
556 near this wall increase more and more. As the bulk temperature grows, and since the right wall
557 (at $x=H$) temperature is maintained at its initial value, a cold boundary layer settles near the
558 right wall where the fluid contracts. The contraction causes an expansion of the bulk and
559 reduces the bulk temperature. The behavior of the fluid is the result of these two competing
560 processes, heating by hot boundary layer and cooling by cold boundary layer. The
561 temperature field is then divided into three distinct zones: two thermal boundary layers
562 associated with large density gradients (Fig. 5) along the vertical walls and the isothermal
563 cavity bulk. Therefore, the temperature and the density profiles exhibit the same behavior,
564 dominated by the piston effect, as in pure fluid [45-46]. In the rest of the paper, we denote as
565 bulk the fluid region, which does not include the boundary layers. The homogeneous bulk
566 temperature and density fields of a supercritical fluid occur at a time that is much shorter than
567 the thermal diffusion time ($t_{PE}=0.23$ s and $t_d=107$ s). They are the signature of the piston effect
568 which was identified a long time ago as responsible for fast heat transport in near-critical pure
569 fluids [47-49]. However, the piston effect plays an important role only for short times because
570 of the disappearance of sharp temperature gradients due to the action of thermal diffusivity.
571 For an advanced time (30s), the system's response, is then markedly different from that
572 observed for shorter times. A similar trend to that of a perfect gas characterized by
573 equilibrium can be depicted. It must be noted that temperature equilibrium is achieved on a
574 time much shorter than the diffusion time. This is probably a consequence of the evolution of
575 mass fraction in the cavity bulk, since w influences the temperature evolution as a source term
576 of the energy equation.

577 The mass fraction field exhibits a different aspect as shown in Fig. 6. In order to explain the
578 typical behavior of the supercritical mixture near the two reactive walls, we focus on the

579 boundary conditions developed in section 2.3. The dependence to temperature and pressure of
580 the adsorption rate can be depicted from Eq. (10). Since the partial derivative of K_2 with
581 respect to pressure is negative (see Fig. 2), the pressure term tends to reduce K_a and as a
582 result, to diminish the adsorbed amount. On the left heated wall, the effect of the temperature
583 increase is amplified by the diverging derivative of K_2 with respect to temperature (see Fig.
584 3), leading to an important amount of Naphthalene adsorbed at the warm side.

585 The phenomenon occurring at the isothermal right wall is totally different. The strong density
586 gradient near the boundary $x=H$ (Fig. 5), generated by the piston effect, goes along with an
587 increase of the amount of Naphthalene neat this reactive wall leading to an increase of the
588 adsorbed quantity. Finally, the strong and homogeneous increase of the pressure, induced by
589 the piston effect in the whole cavity, reduces the adsorbed amount at both reactive walls.

590

591

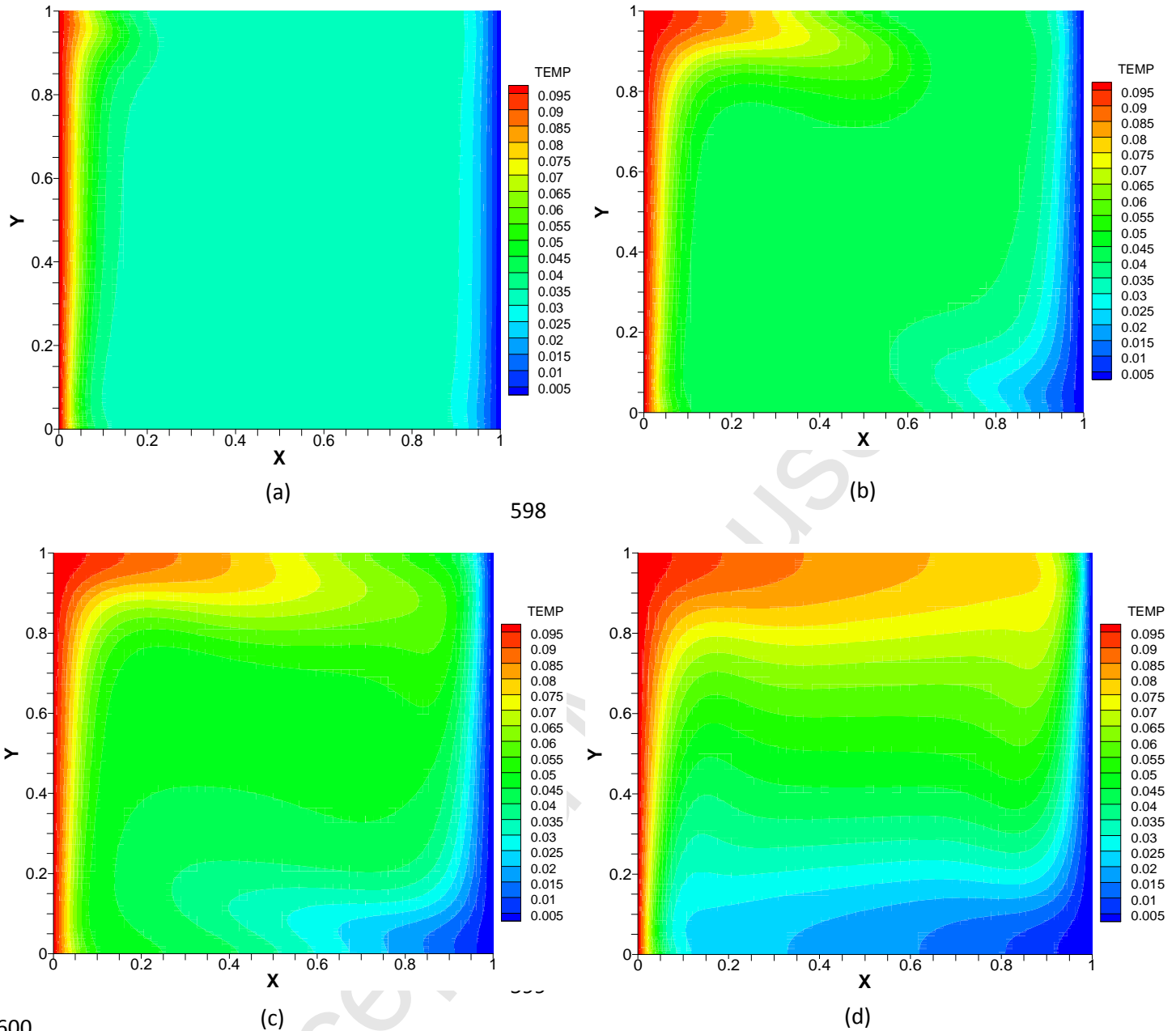
592

593

594

595

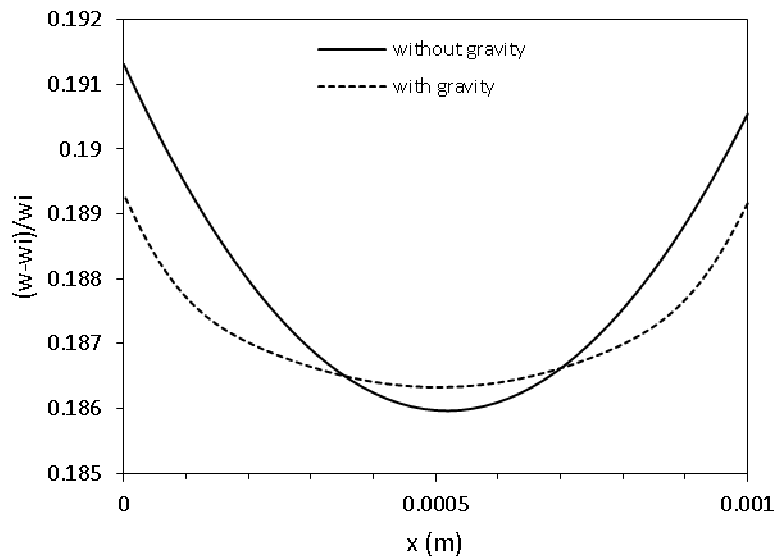
596



601 Fig. 7. Isosurfaces of the temperature variation for several times (a) 1s, (b) 2.5s, (c) 4s and (d) 30s, for $T_i=308.15$ K and
 602 $\Delta T=100$ mK in the presence of gravity

603 We consider now the case when the mixture is subjected to the gravity. In this case,
 604 side heating initiates gravity-driven convection in the fluid phase and the temperature and
 605 density fields obtained are completely two-dimensional on the contrary to the mainly 1D
 606 solutions previously observed in the absence of gravity. In Fig. 7, instantaneous temperature
 607 fields are plotted in the (x,y) plan for several times (1 s, 2.5 s, 4 s and 30 s). During a short
 608 time, the cavity bulk is heated rapidly due to the piston effect. As a result, upstream rises near

609 the left warm surface and a hot spot at the left corner of the cavity can be depicted after 1s and
 610 then it is convected progressively along the top wall for longer times. As in Fig. 4 for $g=0$, a
 611 cool boundary layer forms near the right isothermal wall, due to the piston effect. As a result,
 612 a jet moving down appears near the right wall from 2.5 s. The hot and cold thermal plumes
 613 along the top and the bottom sides develop progressively in time as shown in Fig. 7. We can
 614 clearly see the homogenous increase of the bulk temperature induced by the piston effect.
 615 This aspect is different from the perfect gas case where thermal boundary layer is formed only
 616 near heated side which leads to a single stream [50].



617

618

619

620

Fig. 8. The effect of the gravity on the mass fraction perturbation
 for $T_i=308.15$ K and $\Delta T=100$ mK at $t=500$ s

620

For the sake of comparison and in order to highlight the effect of Earth's gravity, we

621

622

623

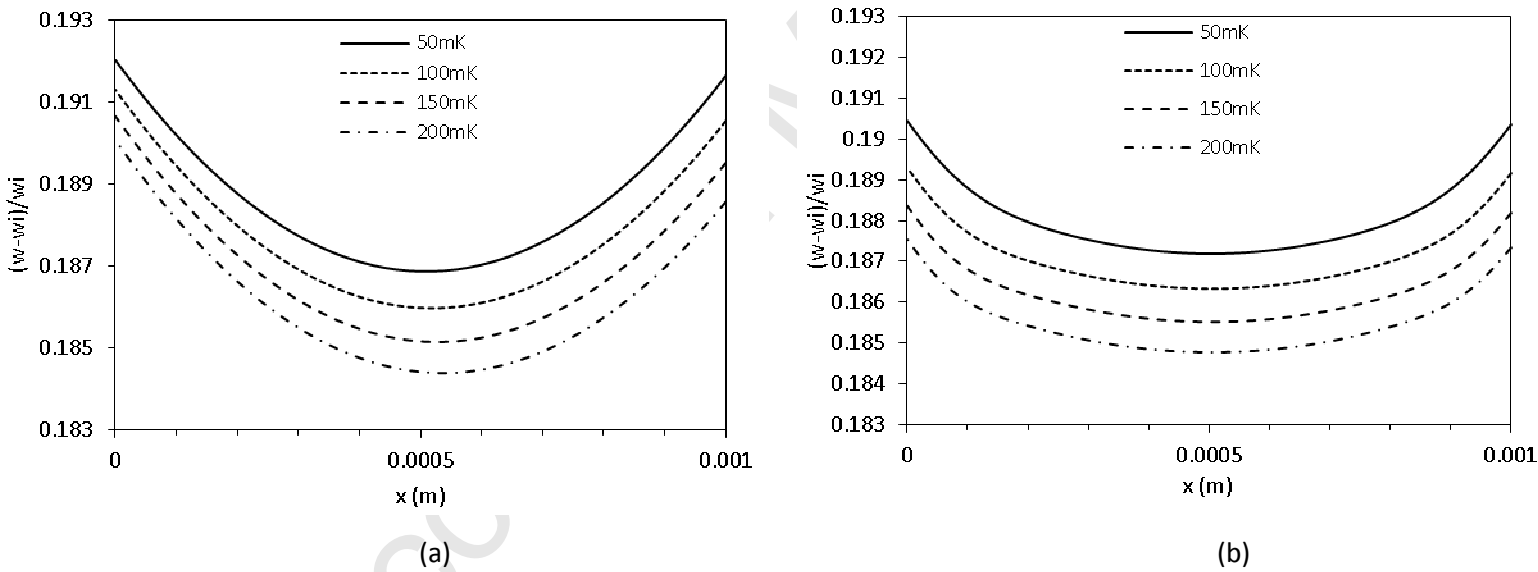
624

625

626

analyze in the following the Naphthalene mass fraction evolution with and without gravity
 (Fig. 8). The difference previously observed between the hot wall and the cold wall has
 disappeared. Gravity in this case tends to balance both sides. Conversely, the amount
 adsorbed is remarkably lower at the two sides (hot and cold) compared to the case without
 gravity. On the other hand, the mass fraction at the cavity centre has increased. These
 observations can be explained as follow:

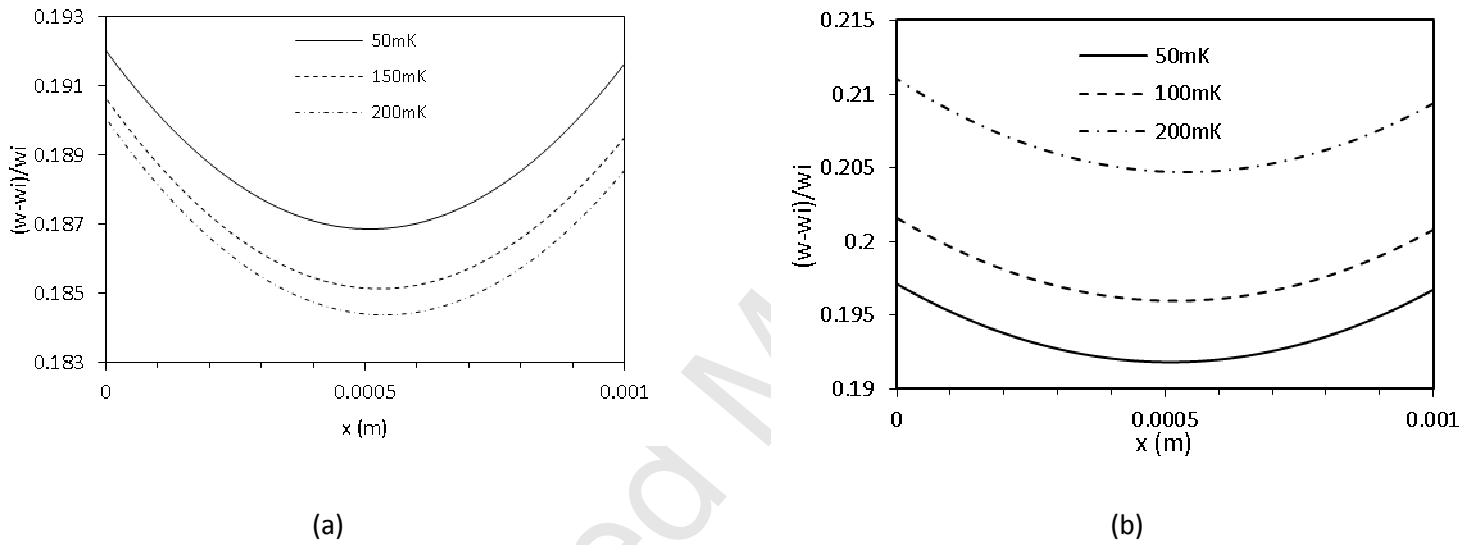
627 For the case without gravity, thermal diffusion process is the only highlighted. The
 628 characteristic time of thermal diffusion is much higher than the time scale of the piston effect.
 629 Such a long process allows keeping a high temperature in the vicinity of the heated wall.
 630 Consequently, as seen above, the divergence of the partial derivative of the equilibrium
 631 constant with respect to temperature near the critical point is believed to affect the mass
 632 fraction rate at the hot side. However, in the case with gravity, density variations generate a
 633 plume which expands upwardly (as shown in Fig. 7). This intensive plume moves hot fluid to
 634 the top boundary and thus decreases the temperature near the warm side. Therefore, the effect
 635 of the derivative with respect to temperature is reduced. Such a phenomenon can explain the
 636 reduction of the mass fraction when gravity is taken into account.



637 Fig. 9. The effect of the solid plate temperature on the mass fraction perturbation without gravity (a) and with gravity (b) for
 638 $T_i=308.15$ K at $t=500$ s

639 The effect of heating intensity is highlighted in Fig. 9 with and without gravity. For the same
 640 proximity to the critical point and the same time, Fig. 9 shows a comparison of the mass
 641 fraction profiles at the cavity mid-height obtained for four values of the temperature rise $\Delta T=$
 642 50mK, 100mK, 150mK and 200mK: the mass fraction decreases with increasing heating. In
 643 the case without gravity, a stronger heating reduces remarkably the mass fraction throughout
 644 the entire volume while keeping the asymmetry of adsorbed amount between the hot and the

645 cold walls (Fig. 9(a)). It can be noted that this asymmetry increases with the heating. A
 646 similar trend can be observed with gravity (Fig. 9(b)). This surprising result can be explained
 647 by the negative pressure term in the adsorption rate K_a (Eq. (10)). Indeed, a stronger heating
 648 of the wall induces a larger thermodynamic pressure increase by the piston effect and, as a
 649 result, a larger value of the pressure term which reduces the parameter K_a . The reduction of
 650 the adsorbed amount at the walls then leads to a smaller mass fraction in the whole cavity.



651
 652 Fig. 10. Influence of the piston effect on the mass fraction perturbation without gravity with (a) $d\text{Ln}K_2/dp \neq 0$ and
 653 $d\text{Ln}K_2/dp = 0$ in Eq. (10) for $T_i = 308.15$ K and $t = 500$ s.

654 This explanation is confirmed by Fig. 10 where a case without the pressure term in Eq.
 655 (10) was tested. We can then observe that with the sole presence of the temperature term, a
 656 stronger heating increases the mass fraction in the entire volume (Fig. 10(b)). Consequently,
 657 the pressure term plays a major role in the expression of the adsorption rate K_a (Eq. (10)) near
 658 the critical point. The evolution of the mass fraction profiles as a function of heating depicted
 659 in Fig. 10(a) is then directly attributable to the piston effect which is responsible for the strong
 660 and homogeneous increase of the pressure in the cavity.

661 3.2 Effect of initial mass fraction

662

663

664

665

666

Table 4

The effect of the initial mass fraction for $T_i=308.15$ K, $\Delta T=100$ mK and $\Delta T=50$ mK at $t=30$ s and without gravity

$\Delta T=100$ mK			
w_i	$w-w_i(x=0)$	$w-w_i(x=H)$	$(w_{x=0}-w_{x=H})/w_{x=0}$
7.6751×10^{-3}	3.93×10^{-4}	3.88×10^{-4}	1.48×10^{-2}
4.22×10^{-3}	1.65×10^{-4}	1.62×10^{-4}	1.97×10^{-2}
2.11×10^{-3}	7.16×10^{-5}	6.99×10^{-5}	2.28×10^{-2}
9.35×10^{-4}	2.95×10^{-5}	2.87×10^{-5}	2.46×10^{-2}
7.6751×10^{-4}	2.39×10^{-5}	2.34×10^{-5}	2.49×10^{-2}
$\Delta T=50$ mK			
w_i	$w-w_i(x=0)$	$w-w_i(x=H)$	$(w_{x=0}-w_{x=H})/w_{x=0}$
7.6751×10^{-3}	3.94×10^{-4}	3.91×10^{-4}	7.44×10^{-3}
4.22×10^{-3}	1.65×10^{-4}	1.64×10^{-4}	9.88×10^{-3}
2.11×10^{-3}	7.15×10^{-5}	7.07×10^{-5}	1.15×10^{-2}
9.35×10^{-4}	2.94×10^{-5}	2.91×10^{-5}	1.24×10^{-2}
7.6751×10^{-4}	2.39×10^{-5}	2.36×10^{-5}	1.25×10^{-2}

667

Table 5

The effect of the initial mass fraction for $T_i=308.15$ K, $\Delta T=100$ mK and $\Delta T=50$ mK at $t=30$ s and with gravity

$\Delta T=100$ mK			
w_i	$w-w_i(x=0)$	$w-w_i(x=H)$	$(w_{x=0}-w_{x=H})/w_{x=0}$
7.6751×10^{-3}	3.78×10^{-4}	3.77×10^{-4}	2.78×10^{-3}
4.22×10^{-3}	1.56×10^{-4}	1.56×10^{-4}	3.11×10^{-3}
2.11×10^{-3}	6.70×10^{-5}	6.67×10^{-5}	3.42×10^{-3}
9.35×10^{-4}	2.74×10^{-5}	2.73×10^{-5}	3.63×10^{-3}
7.6751×10^{-4}	2.22×10^{-5}	2.22×10^{-5}	3.66×10^{-3}
$\Delta T=50$ mK			
w_i	$w-w_i(x=0)$	$w-w_i(x=H)$	$(w_{x=0}-w_{x=H})/w_{x=0}$
7.6751×10^{-3}	3.82×10^{-4}	3.81×10^{-4}	1.83×10^{-3}
4.22×10^{-3}	1.58×10^{-4}	1.57×10^{-4}	2.00×10^{-3}
2.11×10^{-3}	6.76×10^{-5}	6.75×10^{-5}	2.17×10^{-3}
9.35×10^{-4}	2.77×10^{-5}	2.76×10^{-5}	2.28×10^{-3}
7.6751×10^{-4}	2.25×10^{-5}	2.24×10^{-5}	2.30×10^{-3}

669

670

671

672

673

674

675

676

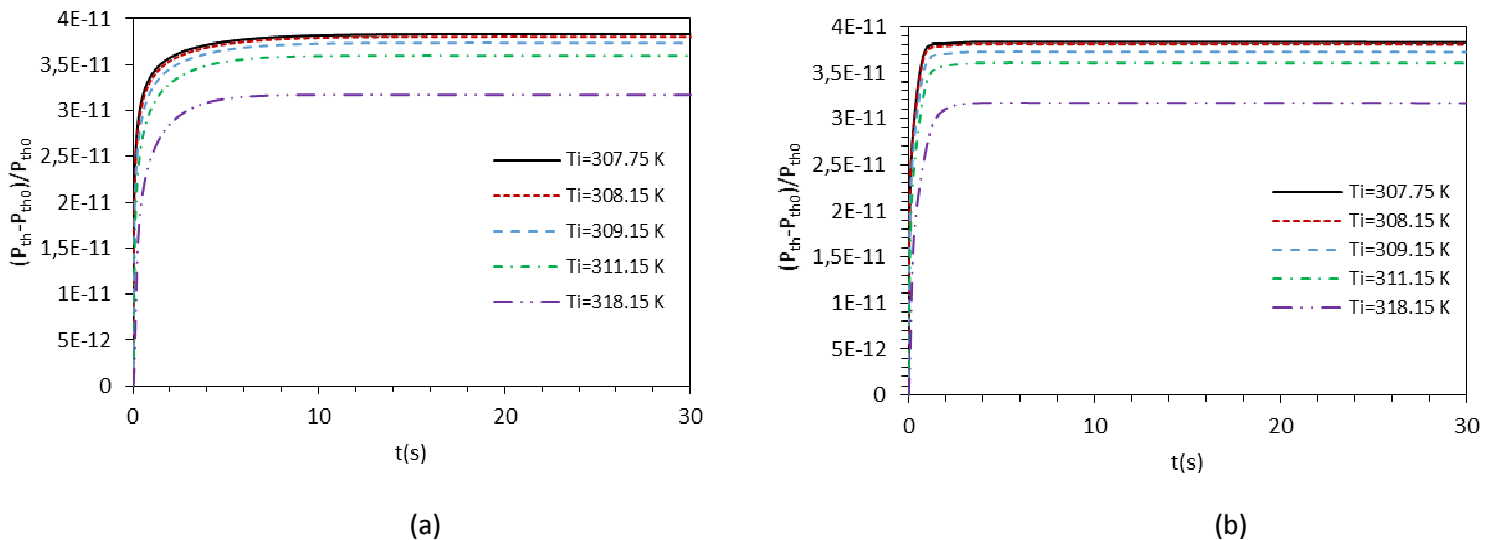
677

The effect of the initial mass fraction on the adsorbed amount at the two walls is reported in Tables 4 and 5 for cases with and without gravity and for two temperature increases $\Delta T=50$ mK and 100 mK. The maximum value of w_i corresponds to the solubility of Naphthalene in CO_2 . We note that the difference between the left and right sides observed in Fig. 8 without gravity can be quantified for each initial mass fraction and for the two temperature increase. Then, the effect of the gravity is confirmed in Table 5 where equilibrium is established between the two sides and only a slight difference can be observed between the heated and the isothermal plates. A detailed analysis of Tables 4 and 5 reveals

678 that, as could be expected, the mass fraction variation at both sides decreases with the initial
 679 mass fraction. To better quantify the difference between the hot and the cold sides, the relative
 680 variation $w_{x=0} - w_{x=H} / w_{x=0}$ is reported in the third column. In the first case, without gravity
 681 and for $\Delta T=100\text{mK}$, a difference of 1.5% can be depicted for the greater initial mass fraction.
 682 Then this difference evolves to 2.5% for the lowest value of w_i . When the heating decreases to
 683 50mK, the difference between the heated and isothermal sides is reduced (0.7% and 1.2% for
 684 high and low initial mass fraction respectively). However, it can be noted that, for both values
 685 of ΔT , the relative difference of adsorbed amount between the hot and cold sides increases
 686 when w_i decreases and the increase is larger for the smaller heating, (71% for $\Delta T=50\text{mK}$ and
 687 66% for $\Delta T=100\text{mK}$). Table 5 shows that the gravity not only lowers the difference between
 688 the two walls (only 0.27% and 0.36% of difference can be observed for higher and lower
 689 initial mass fraction for $\Delta T=100\text{mK}$ and 0.18% and 0.23% for $\Delta T=50\text{mK}$) but also reduces
 690 the effect of the initial mass fraction: the increase between the largest and the smallest values
 691 of w_i is about 31% for $\Delta T=100\text{mK}$ and 26% for $\Delta T=50\text{mK}$. These results then confirm the
 692 balancing influence of the gravity previously depicted by Fig. 8.

693 3.3 Proximity of the LCEP

694



695 Fig. 11. The effect of the proximity to the critical temperature without (a) and with (b) gravity at $\Delta T=100\text{ mK}$.

696

697 The results presented in this section were obtained with an initial mass fraction w_i
 698 corresponding to the solubility of Naphthalene in CO_2 at temperature T_i and density ρ_i . The
 699 values of w_i and the initial pressure P_{thi} calculated using the Peng-Robinson equation are
 700 reported in Table 6.

Table 6Initial mass fraction w_i and pressure P_{thi}

T_i (K)	ρ_i (kg.m ⁻³)	w_i	P_{thi} (MPa)
307.75	470	7.6751×10^{-3}	8.67158154
308.15	470	4.22×10^{-3}	8.73970242
309.15	470	2.11×10^{-3}	8.90942413
311.15	470	9.35×10^{-4}	9.22114740
318.15	470	7.6751×10^{-4}	10.3949472

701

702 A Similar behavior to that described in section 3.1 was observed for the mass fraction for
 703 different initial temperatures T_i and temperature increases ΔT . However, when we move away
 704 from the critical point, the partial derivatives of the equilibrium constant K_2 with respect to
 705 temperature and pressure decrease (Figs. 2 and 3) and thus, the mass fraction at the heated and
 706 isothermal sides are influenced. Moreover, it must be noted that, since the initial mass fraction
 707 w_i is fixed to the value corresponding to the solubility at T_i and ρ_i , the resulting pressure gets
 708 higher as the initial temperature moves away from the critical one. As a consequence, the
 709 initial pressure belongs to the high pressure range where the derivative of K_2 with respect to
 710 pressure is smaller. For all the initial temperatures ($T_i=307.75$ K to $T_i=318.15$ K), the piston
 711 effect generated by the boundary heating induces a fast and strong pressure rise in the entire
 712 volume before the pressure reaches a steady value. When the system is subjected to the
 713 Earth's gravity, convection accelerates the pressure increase (Fig. 11(b)). Yet, with or without
 714 gravity, above the critical point the piston effect becomes less effective and the pressure
 715 plateau for a given ΔT gradually decreases. For $T_i=318.15$ K, steady value is much smaller

716 showing that far enough from the critical point the previously observed effects on temperature
717 and mass fraction will be reduced.

718 The effect on temperature and density can actually be observed in Figs. 12 and 13
719 comparing the instantaneous temperature and density fields near and far from the critical point
720 (for $T_i=307.75$ K and $T_i=318.15$ K). For these two initial temperatures, the characteristic time
721 scales of the piston effect are $t_{PE}=0.19$ s and $t_{PE}=1.26$ s respectively. On the other hand, the
722 characteristic time of thermal diffusion is $t_d=115.7$ s for $T_i=307.75$ K and $t_d=49.23$ s for
723 $T_i=318.15$ K. Therefore, far from the critical point, the piston effect decreases in favor of the
724 thermal diffusion as clearly shown by the temperature field in Fig. 12(b). The boundary layers
725 become thicker and the thermal plumes are larger (Figs 12(b) and 13(b)). The figures also
726 show that, near the critical point ($T_i=307.75$ K), top and bottom plumes reach the opposite
727 plate while the reduction of the piston effect away from the critical point reduces this
728 phenomenon.

729 The lessening of the piston effect depicted by Fig. 11 is confirmed by Tables 7 and 8 which
730 show that the pressure value corresponding to the equilibrium state after $t=30$ s decrease when
731 moving away from the critical point for both temperature increases of 50mK and 100mK and
732 for the two cases with and without gravity effect. It can be also noted that the gravity has a
733 very little influence on the pressure evolution, since very close values are obtained for the
734 pressure with and without gravity. Tables 7 and 8 also show how the proximity to the critical
735 point affects the adsorbed amount at the two reactive walls. In the two cases, with or without
736 gravity, a change in the variation of the mass fraction as a function of initial temperature can
737 be observed for the farest value of T_i . Indeed, the mass fraction at the heated and isothermal
738 plates regularly decreases when the system moves away from the critical temperature up to
739 $T_i=311.15$ K. Then, a strong increase of the mass fraction is observed at $T_i=318.15$ K. A
740 similar behavior change at the highest temperature can also be noted on the relative gap of

741 mass fraction between the two sides. For example, for $\Delta T=100\text{mK}$, the difference between the
 742 two reactive walls increases from about 1.4% at $T_i=307.75\text{ K}$ to 1.6% at $T_i=311.15\text{ K}$ and
 743 then decreases to 1% at $T_i=318.15\text{ K}$. This abrupt behavior change can be attributed both to
 744 the reduction of the piston effect (leading to a smaller pressure increase) and to the decrease
 745 of the derivative of the equilibrium constant K_2 with respect to pressure. These two
 746 phenomena lead to a decrease of the negative pressure term in the adsorption rate expression
 747 (Eq. (10)).

748 **Table 7**
 The effect of the proximity to the critical temperature for $\Delta T=100\text{ mK}$ and $\Delta T=50\text{ mK}$ at $t=30\text{s}$ and without gravity

100 mK				
$T_i\text{ (K)}$	$w-w_i\text{ (x=0)}$	$w-w_i\text{ (x=H)}$	$(w_{x=0}-w_{x=H})/w_{x=0}$	$(P_{th}-P_{th0})/P_{th0}$
307.75	4.09×10^{-4}	4.03×10^{-4}	1.3885×10^{-2}	3.8347×10^{-11}
308.15	3.93×10^{-4}	3.88×10^{-4}	1.4824×10^{-2}	3.8053×10^{-11}
309.15	3.75×10^{-4}	3.69×10^{-4}	1.6061×10^{-2}	3.7326×10^{-11}
311.15	3.71×10^{-4}	3.65×10^{-4}	1.6067×10^{-2}	3.6028×10^{-11}
318.15	4.77×10^{-4}	4.72×10^{-4}	1.0726×10^{-2}	3.1747×10^{-11}
50 mK				
$T_i\text{ (K)}$	$w-w_i\text{ (x=0)}$	$w-w_i\text{ (x=H)}$	$(w_{x=0}-w_{x=H})/w_{x=0}$	$(P_{th}-P_{th0})/P_{th0}$
307.75	4.10×10^{-4}	4.07×10^{-4}	6.9607×10^{-3}	1.9197×10^{-11}
308.15	3.94×10^{-4}	3.91×10^{-4}	7.4364×10^{-3}	1.9046×10^{-11}
309.15	3.75×10^{-4}	3.72×10^{-4}	8.0633×10^{-3}	1.8675×10^{-11}
311.15	3.70×10^{-4}	3.67×10^{-4}	8.0684×10^{-3}	1.8016×10^{-11}
318.15	4.76×10^{-4}	4.73×10^{-4}	5.3793×10^{-3}	1.5852×10^{-11}

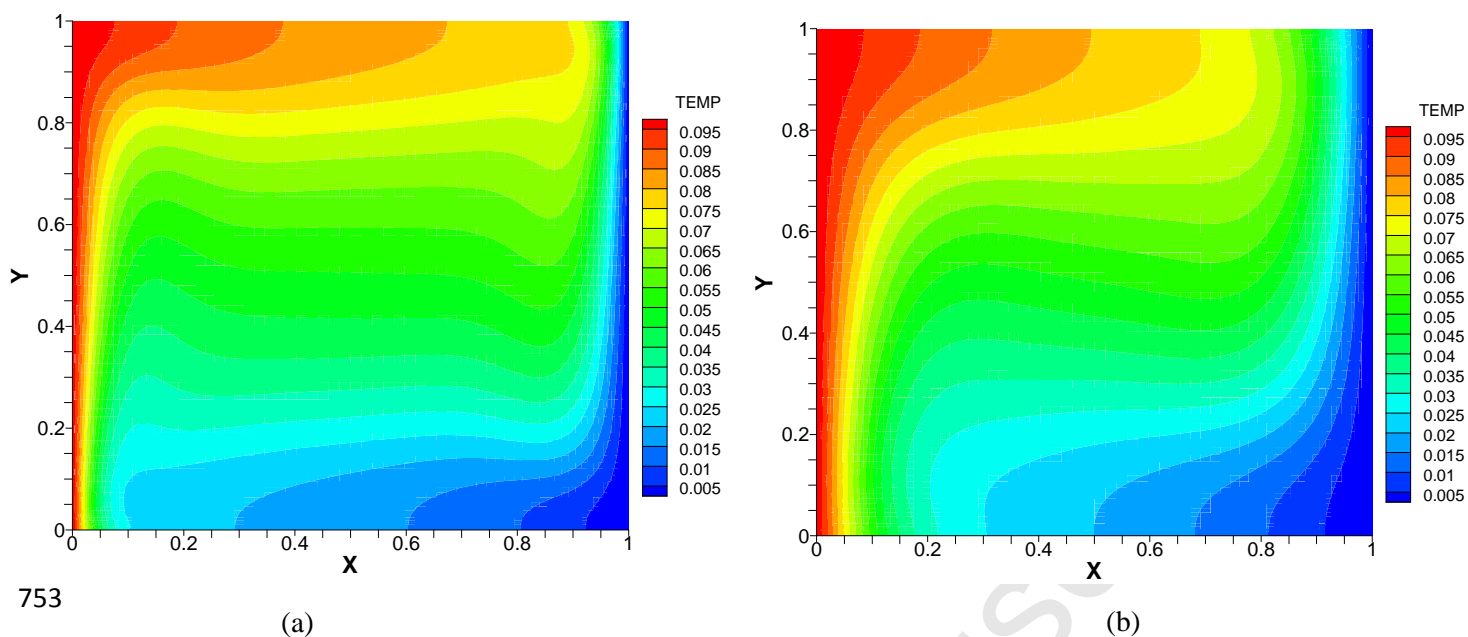
749

750 **Table 8**
 The effect of the proximity to the critical temperature $\Delta T=100\text{ mK}$ and $\Delta T=50\text{ mK}$ at $t=30\text{s}$ and with gravity

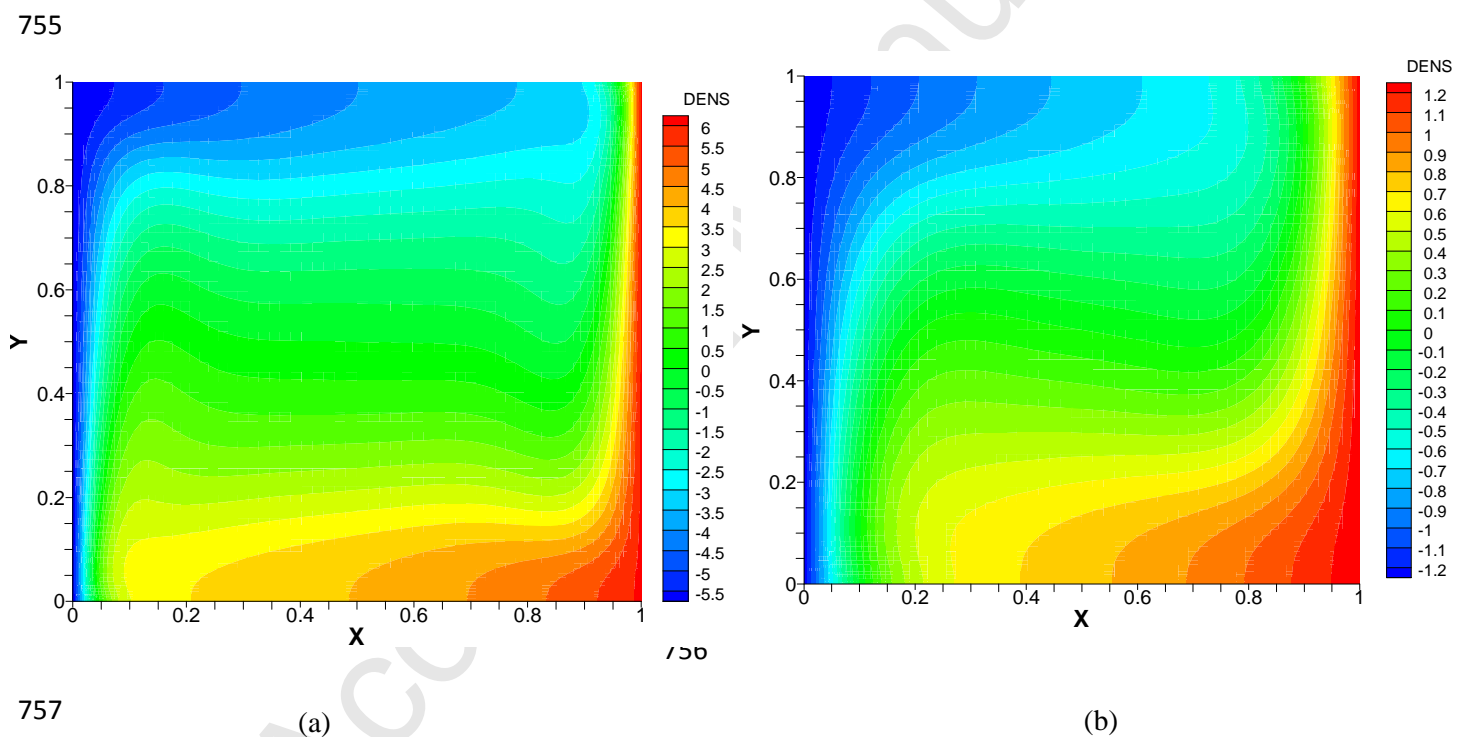
100 mK				
$T_i\text{ (K)}$	$w-w_i\text{ (x=0)}$	$w-w_i\text{ (x=H)}$	$(w_{x=0}-w_{x=H})/w_{x=0}$	$(P_{th}-P_{th0})/P_{th0}$
307.75	3.94×10^{-4}	3.93×10^{-4}	2.6531×10^{-3}	3.8326×10^{-11}
308.15	3.78×10^{-4}	3.77×10^{-4}	2.7778×10^{-3}	3.8036×10^{-11}
309.15	3.58×10^{-4}	3.57×10^{-4}	2.9648×10^{-3}	3.7315×10^{-11}
311.15	3.53×10^{-4}	3.52×10^{-4}	3.0537×10^{-3}	3.6024×10^{-11}
318.15	4.56×10^{-4}	4.55×10^{-4}	2.3868×10^{-3}	3.1752×10^{-11}
50 mK				
$T_i\text{ (K)}$	$w-w_i\text{ (x=0)}$	$w-w_i\text{ (x=H)}$	$(w_{x=0}-w_{x=H})/w_{x=0}$	$(P_{th}-P_{th0})/P_{th0}$
307.75	3.98×10^{-4}	3.97×10^{-4}	1.7511×10^{-3}	1.9199×10^{-11}
308.15	3.82×10^{-4}	3.81×10^{-4}	1.8280×10^{-3}	1.9049×10^{-11}
309.15	3.62×10^{-4}	3.61×10^{-4}	1.9335×10^{-3}	1.8679×10^{-11}
311.15	3.56×10^{-4}	3.55×10^{-4}	1.9657×10^{-3}	1.8020×10^{-11}
318.15	4.59×10^{-4}	4.58×10^{-4}	1.5165×10^{-3}	1.5860×10^{-11}

751

752

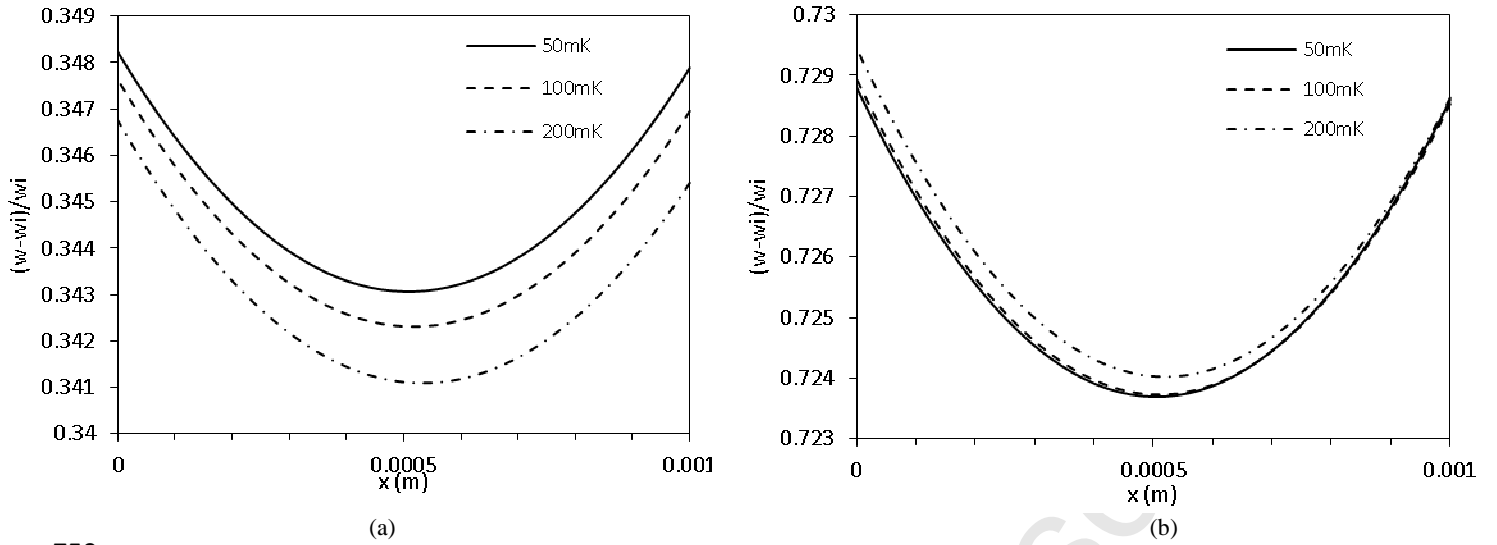


754 Fig. 12. Isosurfaces of temperature with gravity for (a) $T_i=307.75$ K and (b) 318.15 K for $\Delta T=100$ mK at $t=500s$.



757

758 Fig. 13. Isosurfaces of density with gravity for (a) $T_i=307.75$ K and (b) 318.15 K for $\Delta T=100$ mK at $t=500s$



759 Fig. 14. Evolution of the mass fraction with the heating intensity for (a) $T_i=311.15$ K at $t=500$ s and (b) $T_i=318.15$ K at $t=500$ s

760 The consequence of this decrease of the pressure term in Eq. (10) at the highest initial
 761 temperature is depicted by Fig. 14 which shows the mass fraction variation between the two
 762 plates for three temperature increases ($\Delta T=50, 100$ and 200 mK) and two initial temperatures
 763 ($T_i=311.15$ K and 318.15 K). Though the tendency for $T_i=311.15$ K is similar to that shown in
 764 Fig. 10 for $T_i=308.15$ K, the behavior of the mass fraction distribution for $T_i=318.15$ K is
 765 reversed: a stronger heating of the left side increases the mass fraction. The effect is more
 766 remarkable at the heated side than at the isothermal one where the profiles of $\Delta T=50$ mK and
 767 100 mK merge. This behavior change is due to the competition between the derivatives of the
 768 equilibrium constant K_2 with respect to temperature and pressure. Far away from the critical
 769 point, the diverging behaviors of the isothermal compressibility and of the volume expansivity
 770 disappear leading to smaller variations of the derivatives $(\partial \ln K_2 / \partial T)_p$ and $(\partial \ln K_2 / \partial P)_T$
 771 (see Appendix D). Moreover, for a given heating intensity, the pressure increase generated by
 772 the piston effect is much lower for the highest initial temperature. As a result, the negative
 773 pressure term in Eq. (10) becomes negligible and only the temperature effect is highlighted
 774 and causes the enhancement of mass fraction with heating increase.

775

776

777 *3.4 Influence of the Damköhler number*778 **Table 9**779 The effect of the Damköhler number on the mass fraction perturbation for $T_i=308.15$ K and $\Delta T=100$ mK

Da	10^{-4}	10^{-5}	10^{-12}
w-w_i (en x=H)	3.88 x10 ⁻³	3.88 x10 ⁻⁴	2.37 x10 ⁻¹⁰
w-w_i (en x=0)	3.94 x10 ⁻³	3.93 x10 ⁻⁴	2.33 x10 ⁻¹⁰

780

781 The results presented up to now were obtained for a Damköhler number fixed to 10^{-5} .
782 With reference to literature studies, it has been found that the Damköhler number for the
783 adsorption of Naphthalene and other solutes such as toluene or benzene can vary from 10^{-3} to
784 10^{-14} [40-44]. The Damköhler number was estimated using the available data in each research
785 work. For the sake of comparison, three values of the Damköhler number were tested. Similar
786 behaviors to those reported in the previous sections were found for temperature, pressure and
787 mass fraction distribution. Only the mass fraction variations at the heated left side and the
788 isothermal right one are presented in Table 9. The same tendency was found with high mass
789 fraction at the heated plate for all the Damköhler numbers. Whereas the Naphthalene mass
790 fraction is found to be very much smaller for the smallest Damköhler number, increasing Da
791 by a decade results in an increase by a decade of the mass fraction for the larger values of Da.

792 **4. Conclusion**

793

794 In this paper we have presented new results and a detailed analysis of adsorption in a
795 model binary dilute mixture, the Naphthalene-CO₂ mixture, very close to the critical point.
796 The results of this study revealed that sufficiently close to the mixture critical point, the
797 increase of the wall heating remarkably affects the adsorbed amount at the two reactive
798 boundaries and the mass fraction inside the cavity. More precisely, the adsorbed amount, as
799 the bulk mass fraction, is reduced by increasing the wall heating. This peculiar behavior is
800 attributed to the Piston effect, coupled with the divergent character of the derivative of the

801 adsorption equilibrium constant with respect to pressure. Far enough from the critical point,
802 the Piston effect weakens and a classical behavior is observed. Our results also showed that
803 this retrograde adsorption is obtained with and without gravity. However, in the presence of
804 gravity, convection induces large thermal plumes along the hot and cold boundaries and tends
805 to reduce the temperature gradients near the two walls leading to more symmetric profiles of
806 the mass fraction. Finally, the effect of the Damköhler number was studied. The same
807 behavior was found for all the values considered.

808 All the results presented in this paper were obtained for the Naphthalene-CO₂ model
809 mixture. However, we believe that this study can be relevant for many dilute binary mixtures.
810 Indeed, the phenomena observed are due to the divergence of the solvent transport properties
811 (namely the isothermal compressibility and the thermal expansion coefficient) near the critical
812 point leading to the appearance of the Piston effect and to the divergence of the solute
813 thermodynamic properties (such as infinite dilution partial molar volume). And these
814 divergent behaviors occur in a universal way for large classes of systems. Therefore, similar
815 results should be obtained for all binary dilute mixtures involving a non-volatile solute near
816 the solvent's critical point and this kind of dilute mixtures is relevant for many adsorption
817 processes.

818

819 Acknowledgments: The authors acknowledge the financial support from the CNES (Centre
820 National d'Etudes Spatiales).

821 Appendix A

822

823 The ratio of the isobaric and isochoric specific heats for pure CO₂, γ , and for mixture, γ_m ,
824 are calculated from the equation of state as follow:

$$825 \quad \gamma = 1 + \frac{T_i}{C_v \rho_i^2} \left(\frac{\partial P}{\partial T} \right)_\rho^2 \left(\frac{\partial \rho}{\partial P} \right)_T \quad (\text{A.1})$$

826 The derivatives are calculated using the Peng-Robinson equation for pure CO₂:

$$827 \quad \left(\frac{\partial P}{\partial T} \right)_\rho = \frac{(R/M)\rho}{1-b\rho} - f(\rho) \frac{d a}{d T} \quad (\text{A.2})$$

$$828 \quad \text{with } f(\rho) = \frac{\rho^2}{1+2b\rho-b^2\rho^2} \quad \text{and} \quad \frac{d a}{d T} = -1.487422 \frac{(R/M)\beta}{\rho_c} \sqrt{\frac{T_c}{T}} \left[1 + \beta \left(1 - \sqrt{T/T_c} \right) \right]$$

$$829 \quad \left(\frac{\partial \rho}{\partial P} \right)_T = \frac{(1-b\rho)^2}{(R/M)T - a(T)(1-b\rho)^2} \frac{d f}{d \rho} \quad (\text{A.3})$$

$$830 \quad \text{with } \frac{d f}{d \rho} = \frac{2\rho(1+b\rho)}{(1+2b\rho-b^2\rho^2)^2}$$

831 In Eqs. (A2) and (A3), $a(T)$ and b are the coefficients of the Peng-Robinson equation of
832 state written for mass variable in dimensional form.

$$a_i(T) = 1.487422 \frac{(R/M_i)T_{ci}}{\rho_{ci}} \left[1 + \beta_i \left(1 - \sqrt{T/T_{ci}} \right) \right]^2$$

$$833 \quad b_i = 0.253076 \frac{1}{\rho_{ci}}$$

for $i = 1, 2$

834 In a similar way, the capacity ratio of the mixture, γ_m is calculated as follow:

$$835 \quad \gamma_m = 1 + \frac{T_i}{C_v \rho_i^2} \left(\frac{\partial P}{\partial T} \right)_{\rho,w}^2 \left(\frac{\partial \rho}{\partial P} \right)_{T,w} \quad (\text{A.4})$$

836 where the derivatives are calculated using the Peng-Robinson equation of state for the
837 mixture:

$$838 \quad \left(\frac{\partial P}{\partial T} \right)_{\rho,w} = \frac{(R/M_1)\rho \theta(w)}{1-b(w)\rho/\theta(w)} - f(\rho,w) \left(\frac{\partial a}{\partial T} \right)_w \quad (\text{A.5})$$

$$839 \quad \text{with } f(\rho,w) = \frac{\rho^2}{1+2b(w)\rho/\theta(w) - b(w)^2 \rho^2/\theta(w)^2}$$

$$840 \quad \text{and } \left(\frac{\partial a}{\partial T} \right)_w = \frac{d a_1}{d T} (1-w)^2 + 2 \frac{d a_{12}}{d T} w (1-w) + \frac{d a_2}{d T} w^2$$

841 in which the derivatives da_i/dT are calculated as described above for pure component.

$$842 \quad \left(\frac{\partial \rho}{\partial P} \right)_{T,w} = \frac{(1-b(w)\rho/\theta(w))^2}{(R/M_1)T\theta(w) - a(T,w)(1-b(w)\rho/\theta(w))^2 \left(\frac{\partial f}{\partial \rho} \right)_w} \quad (\text{A.6})$$

$$843 \quad \text{with} \quad \left(\frac{\partial f}{\partial \rho} \right)_w = \frac{2\rho(1+b(w)\rho/\theta(w))}{(1+2b(w)\rho/\theta(w) - b(w)^2\rho^2/\theta(w)^2)^2}$$

844 Appendix B

845 The difference of the partial molar internal energies of the two components is expressed by:

$$846 \quad \bar{U}_2(T, \vartheta, y) - \bar{U}_2(T, \vartheta, y) = H_2^0(T_0) - H_1^0(T_0) + Cp_2^0 - Cp_1^0 + \frac{1}{2\sqrt{2b}}COF1 \\ Ln \left(\frac{\vartheta + (1-\sqrt{2})\bar{b}}{\vartheta + (1+\sqrt{2})\bar{b}} \right) + \frac{COF2}{\vartheta^2 + 2\vartheta\bar{b} - \bar{b}^2} \quad (\text{B.1})$$

847 with $H_2^0(T_0)$ and $H_1^0(T_0)$ the perfect gas enthalpy of the two components at $T_0=298.15$ K
848 and y the mole fraction of component 2, calculated from the mass fraction by the formula:

$$849 \quad y = \frac{\left(\frac{M_1}{M_2} \right)_w}{\theta(w)}$$

850 Cp_2^0 and Cp_1^0 are the isobaric heat capacities of components 2 and 1 respectively as perfect
851 gas and their difference is expressed by:

$$852 \quad Cp_2^0 - Cp_1^0 = (A_2 - A_1)(T - T_0) + \frac{1}{2}(B_2 - B_1)(T^2 - T_0^2) + \frac{1}{3}(C_2 - C_1)(T^3 - T_0^3) \\ + \frac{1}{4}(D_2 - D_1)(T^4 - T_0^4)$$

853 Finally:

$$854 \quad COF1 = \left\{ -\frac{1}{b} \frac{db}{dy} \left[\bar{a} - T \left(\frac{\partial \bar{a}}{\partial T} \right)_y \right] + \left(\frac{\partial \bar{a}}{\partial y} \right)_T - T \left(\frac{\partial}{\partial y} \left(\frac{\partial \bar{a}}{\partial T} \right)_y \right)_T \right\}$$

855

$$856 \quad COF2 = \frac{1}{b} \left[\bar{a} - T \left(\frac{\partial \bar{a}}{\partial T} \right)_y \right] \left[\bar{b}(\bar{V}_2 - \bar{V}_1) + \vartheta \frac{d\bar{b}}{dy} \right]$$

$$\frac{d\bar{b}}{dy} = -2\bar{b}_1(1-y) + 2\bar{b}_{12}(1-2y) + 2\bar{b}_2y$$

$$857 \quad \left(\frac{\partial \bar{a}}{\partial y}\right)_T = -2\bar{a}_1(1-y) + 2\bar{a}_{12}(1-2y) + 2\bar{a}_2y$$

$$\left(\frac{\partial}{\partial y}\left(\frac{\partial \bar{a}}{\partial T}\right)_y\right)_T = -2\frac{d\bar{a}_1}{dT}(1-y) + 2\frac{d\bar{a}_{12}}{dT}(1-2y) + 2\frac{d\bar{a}_2}{dT}y$$

858 where \bar{a} , \bar{b} , \bar{a}_i , \bar{b}_i , \bar{a}_{12} and \bar{b}_{12} are the coefficients of the Peng-Robinson equation of state
859 written in molar variables and they are defined by:

$$860 \quad \bar{a}(T, y) = \bar{a}_1(T)(1-y)^2 + 2\bar{a}_{12}(T)y(1-y) + \bar{a}_2(T)y^2$$

$$\bar{b}(y) = \bar{b}_1(1-y)^2 + 2\bar{b}_{12}y(1-y) + \bar{b}_2y^2$$

861 with

$$\bar{a}_i(T) = 1.487422 \frac{RT_{ci}}{(\rho_{ci}/M_i)} \left[1 + \beta_i \left(1 - \sqrt{T/T_{ci}}\right)\right]^2$$

$$862 \quad \bar{b}_i = 0.253076 \frac{1}{(\rho_{ci}/M_i)}$$

$$\bar{a}_{12}(T) = \sqrt{\bar{a}_1(T)\bar{a}_2(T)}(1-k_{12})$$

$$\bar{b}_{12} = \frac{1}{2}(\bar{b}_1 + \bar{b}_2)(1-l_{12})$$

863 In the expression of COF2, the difference of volumes of Naphthalene and CO₂ is expressed
864 by:

$$865 \quad \bar{V}_2 - \bar{V}_1 = (1-2y) \frac{\left[\frac{RT}{(\vartheta - \bar{b})^2} + \frac{2\bar{a}(\vartheta - \bar{b})}{(\vartheta^2 + 2\bar{b}\vartheta - \bar{b}^2)^2} \right] \frac{d\bar{b}}{dy} - \left(\frac{\partial \bar{a}}{\partial y}\right)_T}{\frac{RT}{(\vartheta - \bar{b})^2} - \frac{2\bar{a}(\vartheta + \bar{b})}{(\vartheta^2 + 2\bar{b}\vartheta - \bar{b}^2)^2}} \quad (\text{B.2})$$

866 where ϑ is the molar volume of mixture.

867 Appendix C

868 In the expression of the velocity divergence ($\nabla \cdot V$) (Eq. (8)), the derivatives are calculated as
869 follow:

$$870 \quad \left(\frac{\partial F}{\partial T}\right)_{\rho, w} = \frac{\rho \theta(w)}{1 - b^*(w) \rho / \theta(w)} - f^*(\rho, w) \left(\frac{\partial a^*}{\partial T}\right)_w \quad (\text{C.1})$$

$$871 \quad \text{with } f^*(\rho, w) = \frac{\rho^2}{1 + 2b^*(w)\rho/\theta(w) - b^*(w)^2\rho^2/\theta(w)^2}$$

872 a^* and b^* are those defined for Eq. (5) and are calculated using a_i^* and b_i^* in dimensionless
873 form (see section 2.2).

$$874 \quad \left(\frac{\partial F}{\partial \rho}\right)_{T,w} = -\frac{T\theta(w)}{(1-b^*(w)\rho/\theta(w))^2} + a^*(T,w)\left(\frac{\partial f}{\partial \rho}\right)_w \quad (\text{C.2})$$

$$875$$

$$876 \quad \left(\frac{\partial F}{\partial w}\right)_{\rho,T} = -\frac{\rho T}{(1-b^*(w)\rho/\theta(w))^2} \left[\rho \frac{db^*}{dw} + (1-2b^*(w)\rho/\theta(w)) \left(\frac{M_1}{M_2} - 1 \right) \right]$$

$$877 \quad + f(\rho, w) \left(\frac{\partial a^*}{\partial w}\right)_T - \frac{2a^*(T,w)f(\rho, w)^2}{\rho\theta(w)} \times (1-b^*(w)\rho/\theta(w)) \times \left[\frac{db^*}{dw} - \frac{b^*(w)(M_1/M_2 - 1)}{\theta(w)} \right]$$

$$878 \quad (\text{C.3})$$

879 Appendix D

880 In Eqs. (11)-(12), the volume expansivity, α , the isothermal compressibility, κ , the partial
881 molar volume, \bar{v}_2^m and the partial molar residual enthalpy, $\bar{h}_2^m - h_2^{IG}$, are given by:

$$882 \quad \alpha = \frac{1}{\bar{v}} \left(\frac{\partial \bar{v}}{\partial T}\right)_p = \frac{\frac{\partial \bar{a}}{\partial T} - \frac{R}{\bar{v}(\bar{v}-\bar{b})}}{2\bar{a}(\bar{v}+\bar{b}) - \frac{RT}{\bar{v}(\bar{v}-\bar{b})}} \quad (\text{D.1})$$

$$883 \quad \kappa = -\frac{1}{\bar{v}} \left(\frac{\partial \bar{v}}{\partial p}\right)_T$$

$$884 \quad = \frac{1}{\left(-2\bar{a}(\bar{v}+\bar{b})\bar{v}/(\bar{v}^2+2\bar{v}\bar{b}-\bar{b}^2)^2\right) + RT\bar{v}/(\bar{v}-\bar{b})^2} \quad (\text{D.2})$$

$$885 \quad \bar{v}_2^m = \kappa \bar{v} \left[\frac{\bar{v}-\bar{b}+B}{(\bar{v}-\bar{b})^2} - \frac{(\bar{v}^2+2\bar{v}\bar{b}-\bar{b}^2)A - 2\bar{a}(\bar{v}-\bar{b})B}{(\bar{v}^2+2\bar{v}\bar{b}-\bar{b}^2)^2} \right] \quad (\text{D.3})$$

$$A = 2\bar{a}_{12}, B = 2\bar{b}_{12} - \bar{b}_1$$

$$\bar{h}_2^m - h_2^{IG} = P_{th} \bar{v}_2^m - RT + \frac{(T (\partial \bar{a} / \partial T) - \bar{a})(\bar{v}B - \bar{b} \bar{v}_2^m)}{\bar{b}(\bar{v}^2 + 2\bar{v}\bar{b} - \bar{b}^2)} \quad (D.4)$$

$$+ \frac{1}{2\sqrt{2}\bar{b}} \ln \left(\frac{\bar{v} + (1 - \sqrt{2})\bar{b}}{\bar{v} + (1 + \sqrt{2})\bar{b}} \right) \left[2 \frac{d\bar{a}_{12}}{dT} T - A - \frac{1}{\bar{b}} \left(T \frac{\partial \bar{a}}{\partial T} - \bar{a} \right) B \right]$$

887 References

- 888
889 [1] C. Cagniard de la Tour, Exposé de quelques résultats obtenu par l'action combinée de la chaleur et
890 de la compression sur certains liquides, tels que l'eau, l'alcool, l'éther sulfurique et l'essence de
891 pétrole rectifiée, Annales de Chimie et de Physique. 21 (1822) 127-132.
- 892 [2] D. Aslanidou, C. Tsiptsias, C. Panayiotou, A novel approach for textile cleaning based on
893 supercritical CO₂ and Pickering emulsions, Journal of Supercritical Fluids. 76 (2013) 83-93.
- 894 [3] C. Ventosa, D. Rebiscoul, V. Perrut, V. Ivanova, O. Renault, G. Passemard, Copper cleaning in
895 supercritical CO₂ for the microprocessor interconnects, Micro-electronic Engineering. 85 (2008)
896 1629-1638.
- 897 [4] T. Ito, Y. Otani, H. Inomata, Performance of air filters cleaned by supercritical carbon dioxide,
898 Separation and Purification Technology. 40 (2004) 41-46.
- 899 [5] M.P. Srinivasan, J.M. Smith, B.J. McCoy, Supercritical Fluid Desorption from Activated Carbon,
900 Chemical Engineering Science. 45 (1990) 1885.
- 901 [6] G. Madras, C. Erkey, M. Orejuela, A. Akgerman, Supercritical Fluid Regeneration of Activated
902 Carbon Loaded with Heavy Molecular Weight Organics, Industrial and Engineering Chemistry
903 Research. 32 (1993) 1163.
- 904 [7] S. J. Macnaughton, N. R. Foster, Supercritical Adsorption and Desorption Behavior of DDT on
905 Activated Carbon Using Carbon Dioxide. Industrial and Engineering Chemistry Research. 34 (1995)
906 275-282.
- 907 [8] C. S. Tan, D. C. Liou, Supercritical Regeneration of Activated Carbon Loaded with Benzene and
908 Toluene. Industrial and Engineering Chemistry Research. 28 (1989a) 1222-1226.
- 909 [9] C. S. Tan, D. C. Liou, Desorption of Ethyl Acetate from Activated Carbon by Supercritical Carbon
910 Dioxide. Industrial and Engineering Chemistry Research. 27 (1988) 988-991.
- 911 [10] A.T. Andrews, R.C. Ahlert, D.S. Kosson, Supercritical fluid extraction of aromatic contaminants
912 from a sandy loam soil. Environmental Progress and Sustainable Energy. 9 (1990) 204-210.
- 913 [11] C. Erkey, G. Madras, M. Orejuela, A. Akgerman, Supercritical Fluid Extraction of Heavy
914 Molecular Weight Organic Contaminants from Soil, Environmental Science and Technology. 27
915 (1993) 1225.
- 916 [12] S. Kothandaraman, R.C. Ahlert, E.S. Venkataramani, A.T. Andrews, Supercritical extraction of
917 polynuclear aromatic hydrocarbons from soil. Environmental Progress. 11 (1992) 220-222.
- 918 [13] S.J. Macnaughton, N.R. Foster, I. Kikic, Proc. 3rd Int. Syrup. On Supercritical Fluids, Tome 2,
919 pl, Strasbourg. France, 1994.
- 920 [14] R. Humayun, D.L. Tomasko, High-resolution adsorption isotherms of supercritical carbon
921 dioxide on activated carbon, AIChE Journal. 46 (2000) 2065-2075.

- 922 [15] L.G. Aranovich, D.M. Donohue, Adsorption isotherms for microporous adsorbents. Fuel Energy
923 Abstracts. 37 (1996b) 231.
- 924 [16] C. H. Lochmüller, L.P. Mink, Adsorption isotherms on silica for methanol and 1-hexanol
925 modifiers from supercritical carbon dioxide Journal of Chromatography A. 471: 357-366. DOI:
926 10.1016/S0021-9673(00)94183-9.
- 927 [17] G. Afrane, E. Chimowitz, Adsorption in near-critical binary solvent mixtures: thermodynamic
928 analysis and data. Fluid Phase Equilibria, 111 (1995) 213-238.
- 929 [18] I. Raspo, S. Meradji, B. Zappoli, Heterogeneous reaction induced by the piston effect in
930 supercritical binary mixtures. Chemical Engineering Science. 62 (2007) 4182-4192.
- 931 [19] I. Raspo, B. Zappoli, P. Bontoux, Fast Mass Transfer at a solid-supercritical fluid interface by
932 Piston Effect. Proceedings of 4th ICCHMT May 17-20, Paris-Cachan (2005).
- 933 [20] U. Van Wasen, I. Swaid, G. M. Schneider, Physicochemical Principles and Applications of
934 Supercritical Fluid Chromatography (SFC), Angewandte Chemie, Int. Ed. 19 (1980) 575
- 935 [21] C. R. Yonker, R. W. Wright, S. L. Frye, R. D. Smith, Mechanism of Solute Retention in
936 Supercritical Fluid Chromatography, Supercritical Fluids: Chemical and Engineering Principles and
937 Applications. Squires and Paulaitis, eds., ACS Symposium. 329 (1987) 14.
- 938 [22] J. J. Shim, K. P. Johnston, Adjustable Solute Distribution Between Polymers and Supercritical
939 Fluids, AIChE Journal. 35 (1989) 1097.
- 940 [23] F. P. Schmitz, D. Leyendecker, E. Klesper, Chromatography with Mobile Phases in the Liquid
941 and the Supercritical State, Berichte der Bunsengesellschaft physikalische. 88 (1984) 912.
- 942 [24] E. Klesper, F. P. Schmitz, Gradient Methods in Supercritical Fluid Chromatography,
943 Supercritical Fluids. 1 (1988) 45.
- 944 [25] S. Paolucci, On the filtering of sound from the Navier-Stokes equations. Technical report, Sandia
945 National Laboratories USA, SAND82-8257 (1982).
- 946 [26] Y. Arai, T. Sako, Y. Takebayashi, Supercritical fluids: Molecular Interactions, Physical
947 Properties and new Applications. Springer, Berlin 2002.
- 948 [27] H. Higashi, Y. Iwai, Y. Takahashi, H. Uchida, Y. Arai, Diffusion coefficients of naphthalene and
949 dimethylnaphthalene in supercritical carbon dioxide. Fluid Phase Equilibria. 144 (1998) 269-278.
- 950 [28] C. Nicolas, E. Neau, S. Meradji, I. Raspo, The Sanchez-Lacombe Lattice fluid model for the
951 modeling of solids in supercritical fluids. Fluid Phase Equilibria. 232 (2005) 219-229.
- 952 [29] J. Ouazzani, Y. Garrabos, A new numerical algorithm for low Mach number supercritical fluids,
953 Retrieved october 2007. (available at <https://hal.archives-ouvertes.fr/hal-00142988>).
- 954 [30] I. Raspo, J. Ouazzani, Un algorithme faible nombre de Mach pour la simulation des écoulements
955 de fluides supercritiques par des méthodes spectrales, Proceedings of the 19th Congrès Français de
956 Mécanique, C Rey, P. Bontoux, A. Chrysochoos Eds., ISSN 2103_6225, paper 337-S05 (2009).
- 957 [31] S. K. Jha, G. Madras, Modeling of adsorption equilibria in supercritical fluids, Journal of
958 Supercritical Fluids. 32 (2004) 161-166.
- 959 [32] R.F. Chang, G. Morrison, J.M.H. Levelt Sengers, The critical dilemma of dilute mixtures, Journal
960 of Physical Chemistry. 88 (1984) 3389-3391.
- 961 [33] R.F. Chang, J.M.H. Levelt Sengers, Behavior of dilute mixtures near the solvent's critical point,
962 Journal of Physical Chemistry. 90 (1986) 5921-5927.

- 963 [34] J. M. Vanel, R. Peyret, P. Bontoux, A pseudospectral solution of vorticity-stream function
964 equations using the influence matrix technique. In Morton, K. W., and Baines, M. J. (eds.), Numerical
965 Methods for Fluid Dynamics II. (1986) 463-475.
- 966 [35] S. Hugues, A. Randriamampianina, An improved projection scheme applied to pseudospectral
967 methods for the incompressible Navier-Stokes equations. International Journal for Numerical Methods
968 in Fluids. 28 (1998) 501-521.
- 969 [36] P. Haldenwang, G. Labrosse, S. Abboudi, M. Deville, Chebyshev 3D spectral and 2D
970 pseudospectral solvers for the Helmholtz equation. Journal of Computational Physics. 55 (1984) 115-
971 128.
- 972 [37] I. Raspo, S. Hugues, E. Serre, A. Randriamampianina, P. Bontoux, A spectral projection method
973 for the simulation of complex three - dimensional rotating flows, Computers & Fluids. 31 (2002) 745-
974 767.
- 975 [38] G. Accary, I. Raspo, P. Bontoux, B. Zappoli, An adaptation of the low Mach number
976 approximation for supercritical fluid buoyant flows, Comptes Rendus Mecanique. 331 (2005) 397-
977 404.
- 978 [39] D. Ameer, I. Raspo, Numerical simulation of the Poiseuille-Rayleigh-Bénard instability for a
979 supercritical fluid in a mini-channel, Computational Thermal Sciences. 5 (2013) 107-118.
- 980 [40] F. A. Aisien, A. Amenaghawon, A. Adinkwuye, Batch study, equilibrium and kinetics of
981 adsorption of naphthalene using waste tyre rubber granules. Journal of Xenobiotics. 4 (2014) 2264.
- 982 [41] B. Cabal, C. Ania, J. Parra, J. Pis, Kinetics of naphthalene adsorption on an activated carbon :
983 Comparison between aqueous and organic media. Chemosphere. 76 (2009) 433-438.
- 984 [42] C. Long, J. Lu, A. Li, D. Hu, F. Liu, Q. Zhang, Adsorption of naphthalene onto the carbon
985 adsorbent from waste ion exchange resin : Equilibrium and kinetic characteristics. Journal of
986 Hazardous Materials. 150 (2008) 656-661.
- 987 [43] S. Lucas, M. Calvo, C. Palencia, M. Cocero, Mathematical model of supercritical CO₂ adsorption
988 on activated carbon effect of operating conditions and adsorption scale-up. Journal of Supercritical
989 Fluids. 32 (2004) 193-201.
- 990 [44] Q. Shi, A. Li, Z. Zhu, B. Liu, Adsorption of naphthalene onto a high-surface-area carbon from
991 waste ion exchange resin. Journal of Environmental Sciences. 25 (2012) 188-94.
- 992 [45] B. Zappoli, S. Amiroudine, P. Carles, J. Ouazzani, Thermoacoustic and buoyancy-driven
993 transport in a square side-heated cavity filled with near-critical fluid. Journal Fluid Mechanics. 316
994 (1996) 53-72.
- 995 [46] G. Accary, I. Raspo, P. Bontoux, B. Zappoli, Three-dimensional Rayleigh-Bénard instability in a
996 supercritical fluid, Comptes Rendus Mecanique. 332 (2004) 209-216.
- 997 [47] H. Boukari, J. N. Shaumeyer, M. E. Briggs, R. W. Gammon, Critical speeding up in pure fluids.
998 Physical Review A. 41 (1990) 2260-2263.
- 999 [48] A. Onuki, H. Hao, R. Ferrell, A. Fast adiabatic equilibration in a single- component fluid near the
1000 liquid-vapor critical point. Physical Review A. 41 (1990) 2256-2259.
- 1001 [49] B. Zappoli, D. Bailly, Y. Garrabos, B. Le Neindre, P. Guenoun, D. Beysens, Anomalous heat
1002 transport by the piston effect in supercritical fluids under zero gravity. Physical Review A. 41 (1990)
1003 2264-2267.

1004 [50] I. P. Vadim, E. B. S. (Ed.), 10-15 September 2000. Simulation of naturel convection in a side-
1005 heated cavity with a near-critical fluid. No. 229-234. Proceedings of the First International Symposium
1006 on Microgravity Research & Application in Physical Sciences & Biotechnology.
1007

Accepted Manuscript